MONTE CARLO SIMULATIONS OF SOLID WALLED

PROPORTIONAL COUNTERS WITH DIFFERENT SITE SIZE FOR HZE

RADIATION

A Thesis

by

XUDONG WANG

Submitted to the Office of Graduate Studies of
Texas A&M University
in partial fulfillment of the requirements for the degree of

MASTER OF SCIENCE

December 2006

Major Subject: Health Physics

MONTE CARLO SIMULATIONS OF SOLID WALLED

PROPORTIONAL COUNTERS WITH DIFFERENT SITE SIZE FOR HZE

RADIATION

A Thesis

by

XUDONG WANG

Submitted to the Office of Graduate Studies of
Texas A&M University
in partial fulfillment of the requirements for the degree of

MASTER OF SCIENCE

Approved by:

Chair of Committee,   Leslie A. Braby
Committee Members,   Rainer Fink
                     W. Dan Reece
Head of Department,   William E. Burchill

December 2006

Major Subject: Health Physics

ABSTRACT

Monte Carlo Simulations of Solid Walled Proportional Counters
with Different Site Size for HZE Radiation. (December 2006)
Xudong Wang, B.S., Lanzhou University;
M.S., Institute of Modern Physics, Chinese Academy of Sciences
Chair of Advisory Committee: Dr. Leslie A. Braby

Characterizing high z high energy (HZE) particles in cosmic radiation is of importance for the study of the equivalent dose to astronauts. Low pressure, tissue equivalent proportional counters (TEPC) are routinely used to evaluate radiation exposures in space. A multiple detector system composed of three TEPC of different sizes was simulated using the Monte-Carlo software toolkit GEANT4. The ability of the set of detectors to characterize HZE particles, as well as measure dose, was studied.

HZE particles produce energetic secondary electrons (δ-rays) which carry a significant fraction of energy lost by the primary ion away from its track. The range and frequency of these delta rays depends on the velocity and charge of the primary ion. Measurements of lineal energy spectra in different size sites will differ because of these delta ray events and may provide information to characterize the incident primary particle.

Monte Carlo calculations were accomplished, using GEANT4, simulating solid walled proportional detectors with unit density site diameter of 0.1, 0.5 and 2.5 μm in a uniform HZE particle field. The simulated spherical detectors have 2 mm thick tissue equivalent walls. The uniform beams of 1 GeV/n, 500 MeV/n and 100 MeV/n ^{56}Fe, ^{28}Si, ^{16}O, ^{4}He and proton particles were used to bombard the detector. The size effect of such a detector system was analyzed with the calculation results.

The results show that the y vs. yf(y) spectrum differs significantly as a function of site size. From the spectra, as well as the calculated mean lineal energy, the simulated particles can be characterized. We predict that the detector system is capable of

characterizing HZE particles in a complex field. This suggests that it may be practical to use such a system to measure the average particle velocity as well as the absorbed dose delivered by HZE particles in space. The parameters used in the simulation are also good references for detector construction.

ACKNOWLEDGEMENTS

I would like to thank my advisor, Dr. Braby, for his patient guidance and support throughout the course of this research. His time and effort are greatly appreciated. I would also like to thank Dr. Reece for taking the time to revise my project paper and the thesis, as well as giving me constructive criticism. Special thanks to Dr. Lijun Qin and Dr. Zhiqiang Chen for much help in GEANT4. I also appreciate the support of Dr. John Poston, Dr. John Ford, Amy Caldwell, Mary Helen Coady, the faculty and staff of the Department of Nuclear Engineering.

I also want to extend my gratitude to all of my friends who have been encouraging me along the way. Finally, thanks to my parents and sisters for their support and encouragement, and my wife for her patience and love.

TABLE OF CONTENTS

LIST OF FIGURES

LIST OF TABLES

CHAPTER I

INTRODUCTION

Since Wilhelm K. Roentgen discovered x-rays in 1895, advances in technology have lead to the need for with more and more development in the area of radiation measurement. For example, the spectrum of radiation exposure received by astronauts due to cosmic ray is of interest, especially at the time when human exploration beyond the earth's magnetosphere is again being planned. The present study of radiation biology requires measuring the average energy deposited per unit mass (*absorbed dose*), by ionizing radiation in specific small targets. Moreover, to predict the effects, we need to characterize the radiation because the relative biological effectiveness (RBE) may differ for different types of radiation when they deliver the same dose. These are the two primary concerns in microdosimetry measurement of cosmic rays.

Microdosimetry is 'the systematic study and quantification of the *spatial* and *temporal* distribution of absorbed energy in irradiated matter' (Rossi and Zaider 1996). The measurement is focused on the energy deposited in a short segment of a charged particle track. It is most useful at low doses because the difference between energy distribution in individual sites and the average becomes significant due to track structure. The microdosimetry method can be applied not only to radiation biology and related fields, but also on microelectronics and large molecules in chemical processes.

The target size relevant for microdosimetry normally varies from DNA molecules (~10 nm) to a cluster of cells (~1 mm). The target size should be chosen carefully according to the research interest. When site size changes, the portion of the track segment involved in measurement changes. Thus, the average of deposited energy may differ. The size effect is critical in HZE measurement, because a large portion of the energy is carried away from the primary track by energetic secondary electrons (δ-rays). The fraction of the energy deposited by the primary particle varies with the size.

_____
This thesis follows the style of Health Physics.

High-energy heavy charged (HZE) particles are a small part of the cosmic ray spectrum but contribute a large portion to the total equivalent dose because of their higher quality factors. For example, the *radiation weighting factor* (that has been called *quality factor*) for heavy particles is 20, while it is 1 for photons and electrons, and 5 for protons (ICRP 1990). So measuring the imparted energy only is not enough to evaluate the biology effect. We need to have information to characterize incident particles by charge, mass and energy. In this research, the particle characterization focuses on HZE particles, including helium ions, and protons.

Low pressure, tissue-equivalent, proportional counters (TEPC) are currently used to evaluate radiation exposures in the space shuttle and space station. They measure the energy imparted by the radiation in a simulated tissue volume. They give direct information about the absorbed dose and an estimate of the effective dose, which is based on the estimate of quality factor (Q) from the relationship between the distribution of deposited energy and the distribution of LET. But a TEPC can not give a complete spectrum of the radiation field.

There are also instruments, such as mass spectrometer and particle telescopes, which can be used to obtain information of charge, mass and energy of the incident particle, but they are typically large and awkward and not appropriate for routine radiation dosimetry. Furthermore, they are only capable of analyzing a specific portion of the radiation spectrum. Several instruments are needed to measure the total absorbed dose, and this approach generally requires complicated data analysis because of the overlapping response functions of the instruments.

To improve the dose and equivalent dose measurement of HZE particles, we propose to take advantage of the relationship between *lineal energy* and the site size to develop a multi-detector system. The system may consist of three to four proportional counters simulating different sized sites. Each detector gives a different spectrum of lineal energy distribution. The degree of discrepancies between these spectra differs for particles with different kinetic energy and mass. It is anticipated that the differences in

the spectra measured by the three detectors will provide additional information on the incident particle velocities and mass.

Before building any of these detectors, we have a few questions to answer about their physical design. What kind of detector should we use, walled or grid-walled (wall-less) detector? What sizes should we choose? How much measurable difference do these detectors have to particles with different charge and energy? Monte-Carlo simulations are necessary to study the possibility of the proposed method. This study focuses on walled detectors. Monte-Carlo toolkit GEANT4 is used in the simulation.

CHAPTER II

BACKGROUND

Charged particles deposit energy by two major interactions with matter, ionization and excitation. A new term 'ionizing radiation' was introduced to refer to electromagnetic radiation and atomic fragments (electrons and nuclear constituents) involving these two processes (Rossi and Zaider 1996). Secondary electrons generated by ionization, and nuclear fragment generated in nuclear reaction, carry energy away from the primary particle and deposit it by ionization and excitation again. Uncharged particles, such as photons and neutrons generated by bremsstrahlung effect and nucleus deexcitation, deposit energy indirectly by producing charged particles, such as electrons and protons. So, for all the radiations, the lesions to cells are induced, finally, by ionization and excitation.

The *absorbed dose* and *linear energy transfer* (LET, defined as the loss of energy per unit distance along the path of a charged particle) (p179 Attix 1986) are most commonly used quantities to predict the lesions. Along with absorbed dose, the microscopic pattern of energy distribution is used to evaluate the relative biological effectiveness (RBE). The biological effect might be different for radiations which have different primary-secondary track structure, with same absorbed dose. For example, HZE particles generate more frequent δ-ray tracks around the primary track than protons with the same speed. The lesions to the cells along the track are more severe in this case. This property can be described by LET. But there are limitations to describe radiation type and RBE using LET.

Firstly, LET is as a quantity describing the average property of incident particle rather than the interaction with the individual irradiated target. Energy loss does not always equal to local energy deposition. For a small target or a high energy particle, δ-rays escape from the target and deposit energy out of the site. The energy deposited in target is smaller than total energy loss. The dose will be overestimated unless δ-ray CPE (charge particle equilibrium) exists. Target size is not a good measure of track length,

either. The difficulty comes mainly from range straggling. Another situation is that for a large target or a low energy particle, the dose might be underestimated if there are tracks begin or end within the site. When the LET has observable changes within the target, the situation becomes more complicate. Furthermore, same LET does not mean same spatial distribution of dose. LET is a strong function of particle velocity and charge, and the energy distribution of δ-rays is mainly determined by particle velocity. So particles with same LET may have different δ-ray range, which results in different spatial dose distribution.

Secondly, as a non-stochastic average quantity, LET does not show the energy deposition fluctuations and range straggling. There are considerable difficulties in measuring these two factors experimentally. We can see that LET is a macro-scale quantity and thus awkward to use when describing a micro-scale event. Such events are related to details of track structure at the cellular level.

Lineal Energy

The limitations of average quantities lead to the introducing of stochastic quantities, such as *lineal energy*, *y* and the *specific energy*, *z*, which are of primary importance in order to interpret the data obtained by a proportional counter. *Linear energy* will be frequently used in this paper. It is defined as the quotient of ε by $\bar{l}$:

$$y = \frac{\varepsilon}{\bar{l}}$$ (2.1)

where ε is the energy imparted to matter in a volume by a single energy deposition event and $\bar{l}$ is the mean chord length (MCL) in that volume (Rossi and Zaider 1996). The most commonly used unit of *y* is keV/μm. The MCL in a convex site is

$$\bar{l} = \frac{4V}{S}$$ (2.2)

where V is the volume and S is the surface of the site (Rossi and Zaider 1996). The MCL of a sphere is

$$\bar{l} = \frac{2}{3}d \qquad (2.3)$$

where d is the diameter of the sphere. Because $\bar{l}$ comes from the random distribution of chord length and the ε comes from a single energy deposition event, y is a stochastic quantity. It is a quantity describing the micro-scale energy deposition in site. Since it does not use average track characteristics to evaluate the effect in the site, it does not have the limitations mentioned above. Note that ε and $\bar{l}$ will change with the diameter of the volume. So for the same event, y measured in different size site will differ. This is a property of lineal energy that LET does not have. The target size should be chosen carefully in order to interpret irradiation effect properly. It is also a critical property that we will take advantage of in this paper, and will be discussed in *Size Effects*.

Microdosimetric Spectrum

Because y is a random variable with a different value for each individual event, the distribution of events is formulated by the probability density of y, f(y) (Fig. 2.1). But a linear representation, f(y) vs y, is not convenient to express the relationship, because f(y) is a function of y which ranges over 8 orders of magnitude (Rossi and Zaider 1996). The most commonly used representations of the spectra are $yf(y)$ vs log(y), and $yd(y)$ vs log(y) (Figs. 2.2 and 2.3).

The probability density of dose d(y) can be calculated:

$$d(y) = \frac{yf(y)}{y_F} \qquad (2.4)$$

where y_F is called the *frequency mean lineal energy*. It is the first moment of y.

$$y_F = \bar{y} = \int yf(y)dy \qquad (2.5)$$

The ratio of the second and first moment of y, y_D, is called *dose mean lineal energy*.

$$y_D = \frac{\overline{y^2}}{\bar{y}} = \frac{1}{y_F}\int y^2 f(y)dy = \int yd(y)dy \qquad (2.6)$$

f(y) vs. y
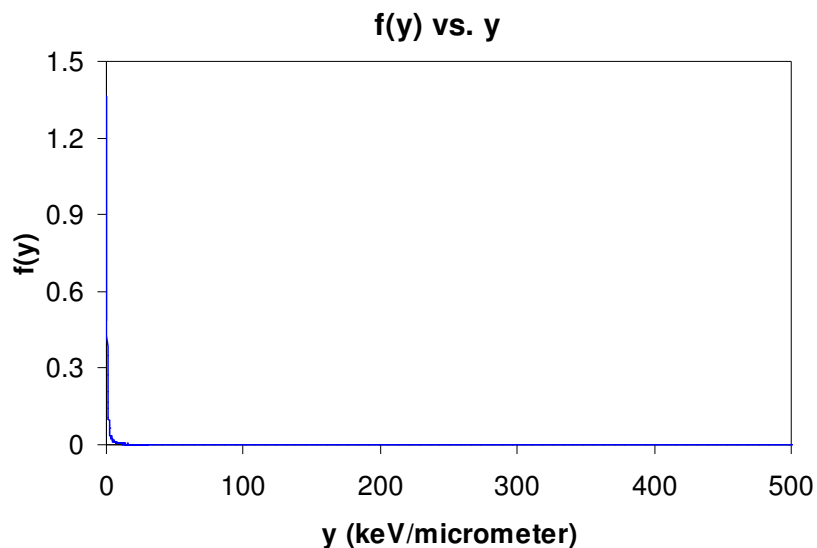
Fig. 2.1. Calculated microdosimetric spectrum, f(y), for energy deposited by 500 MeV $^{56}Fe^{26+}$ in a 0.1 μm diameter spherical detector with 2 mm tissue equivalent wall. We can see that details of the distribution are 'hidden' by this linear representation.
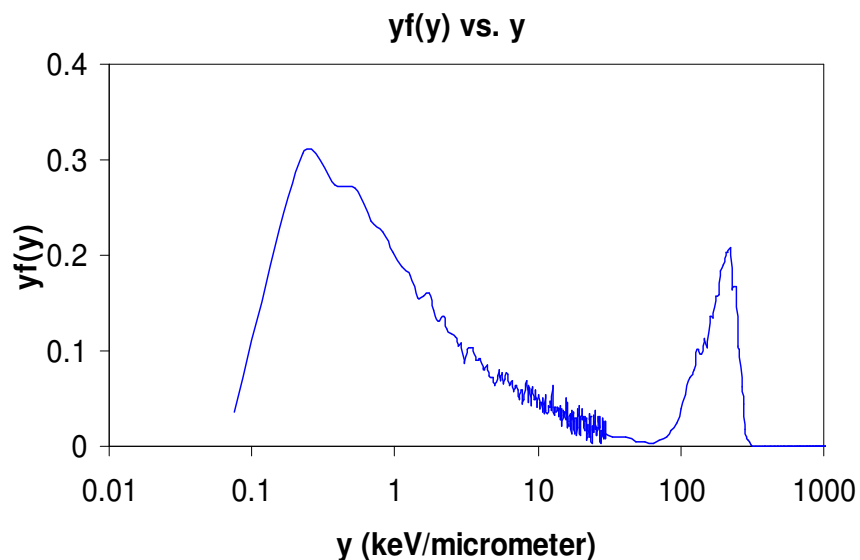
yf(y) vs. y

Fig. 2.2. A semi-log representation of the same spectrum in Fig. 2.1. Note that the ordinate has been multiplied by y. The area under the curve in a range of y is proportional to the fraction of events in this range.

In an $yf(y)$ vs log(y) plot, the area under the curve delimited by any two values of y is proportional to the fraction of events in this range (Fig. 2.2). This plot is commonly used to represent the frequency of events. In a $yd(y)$ vs log(y) plot, the area under the curve delimited by any two values of y is proportional to the fraction of dose delivered by events with lineal energies in this range (Fig. 2.3). This is commonly used to represent the distribution of dose.

yd(y) vs. y
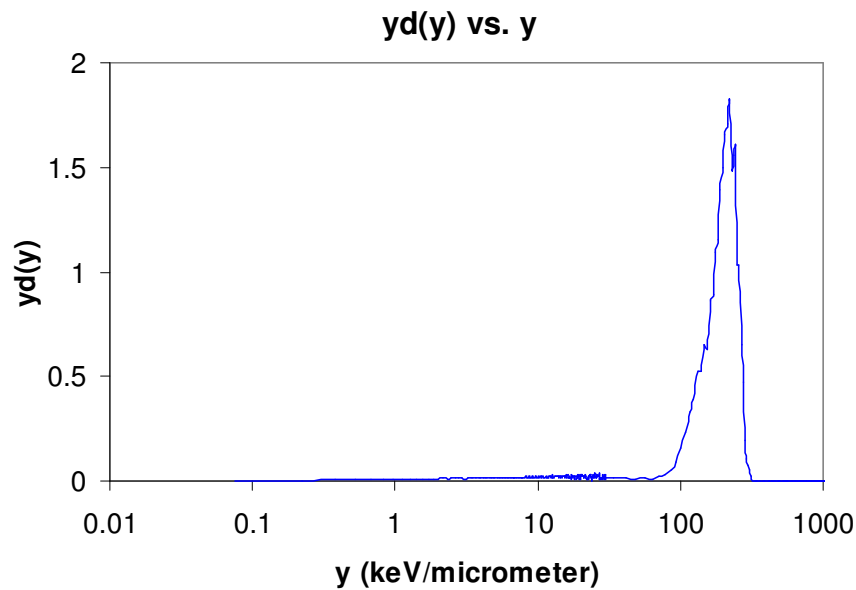
Fig. 2.3. The semi-log representation of the dose distribution, d(y), for the same spectrum in Fig. 2.1. Note that the ordinate is $yd(y)$. The area under the curve in a range of y is proportional to the fraction of dose in this range.

Normalization is of importance in visualizing each of the different representations. Normalization can provide convenient comparison of distributions from different measurements. By definition, f(y) is normalized to 1 energy deposition event:

$$\int_0^\infty f(y)dy = 1 \tag{2.7}$$

And similarly,

$$\int_0^\infty d(y)dy = 1 \tag{2.8}$$

To get the same normalization in a plot of a logarithmic scale of y, the following transformation is employed:

$$f(y)dy = yf(y)d\ln(y) = (\ln 10)yf(y)d(\log y) \tag{2.9}$$

Using the relationship $\Delta(\log y) = \dfrac{1}{B}$, where B is the increments per decade ($y = y_0 \cdot 10^{n/B}$), then the normalization becomes:

$$\int_0^\infty yf(y)d(\ln y) = \ln 10 \int_0^\infty yf(y)d(\log y) \approx \frac{\ln 10}{B}\sum_{i=0}^\infty y_i f(y_i) = 1 \tag{2.10}$$

According to the same method, the normalization of d(y) becomes:

$$\int_0^\infty yd(y)d(\ln y) = \ln 10 \int_0^\infty yd(y)d(\log y) \approx \frac{\ln 10}{B}\sum_{i=0}^\infty y_i d(y_i) = 1 \tag{2.11}$$

Practically, we need apply the normalization and make the comparison in histogram, there are a few concerns which need to be mentioned:

1. The spectrum obtained is an array containing discrete data. Normally, they are counts in discrete lineal energy ranges, which are fragments of a continuous linear ordinate. So the fraction of events occurring in each range is the integral of probability density function (PDF) in this range, but PDF itself:

$$P(\Delta y_i) = \int_{\Delta y_i} f(y)dy \approx f(y_i) \cdot \Delta y_i \tag{2.12}$$

where $f(y_i)$ is the PDF at y_i, Δy_i is the small lineal energy range at y_i, and y_i is normally assigned the average lineal energy of the range. Similarly, we have:

$$P(\Delta y_i) = \int_{\Delta y_i} d(y)dy \approx d(y_i) \cdot \Delta y_i \tag{2.13}$$

2. When we use a linear segmented data array to get the semi-log plot, the appearance of a spectrum of the normalized data changes dramatically if a spectrum has a different start point (data starts from the lowest lineal energy greater than zero). When y goes down to 0, log(y) becomes negative infinity rapidly. $\Delta\log(y_i)$ with low y_i is much larger than that with high y_i when y decreases linearly. This in turn affects the area under

the curve near the start point. The simple method is to use same *y* scale starting from the same point to get good curve normalization. This problem will be discussed in Chapter III.

Proportional Counter

The low-pressure proportional counter was developed and first introduced to measure energy imparted in micrometer scale sites in early 1950s, particularly by H.H. Rossi and his co-workers (Rossi et al. 1961; Rossi and Rosenzweig 1955). A proportional counter measures energy deposition due to ionization from ionizing radiations that interact with it. It simulates a small volume of tissue by a large volume of gas at low density. The two volumes should have same energy deposition if an identical charged particle goes through them. For a tissue sphere of diameter d_t, with density ρ_t, and a gas sphere of diameter d_g, with density ρ_g, the required condition of equivalent energy deposition is (ICRU 1983):

$$\Delta E_t = (S/\rho)_t \rho_t d_t = (S/\rho)_g \rho_g d_g = \Delta E_g \tag{2.14}$$

where ΔE_t and ΔE_g are the mean energy losses from the charged particle in tissue and gas and $(S/\rho)_t$ and $(S/\rho)_g$ are the mass stopping powers. If the atomic composition of tissue and gas are identical, and if the mass stopping powers are independent of density then the requirement becomes:

$$\rho_g = \frac{1}{k_{gt}} \rho_t \tag{2.15}$$

where k_{gt} is the ratio of gas to tissue diameter, d_g/d_t. The volume of the gas sphere is larger by a factor k_{gt}^3 and the mass by a factor k_{gt}^2. So for a single energy deposition event, the dose to the gas sphere is smaller by a factor of $1/k_{gt}^2$. However, if the spheres are in a uniform field, the does is the same for both. This is possible because the cross section of the detector is larger by a factor k_{gt}^2, thus the number of traversing particles is also increased by k_{gt}^2.

Size Effects

HZE particles can produce many energetic δ-rays, which will carry a significant fraction of the energy, lost by the primary ion, away from its track. For a typical proportional counter simulating a spherical piece of tissue with 2 μm diameter, a 600 MeV/nucleon $^{56}Fe^{26+}$ particle going through will generate δ-rays, with the maximum energy of 1.75 MeV, which are energetic enough to escape from the site and travel up to 8000 μm away from the path of the iron ion (Metting et al. 1988). The lineal energy measured for the same particle in a different size site will differ because of these delta ray events. On the other hand, the mean energy and range of these delta rays depends on the velocity of the primary ion and the number of δ-rays depends on its charge. As mentioned above, particles with different velocity and charge may have the same LET, but will have different delta ray ranges, so the frequency mean lineal energy measured in a given size site will be different (Guetersloh et al. 2004). As a result of these effects, the differences in the measurement may provide information to characterize the incident primary particles. We can study the mean lineal energy as a function of particle energy (velocity) and charge. Comparison of the results of a series of such calculations for different site sizes can be used to characterize particles. This is the cornerstone of theory in this study on multi-size detector system.

Wall Effects

The proportional counter conventionally built for microdosimetry use has walls made of tissue-equivalent plastic with the cavity filled with tissue-equivalent gas. The most commonly used shapes are sphere and cylinder. If the cylinder's height is same to the diameter, it has the same MCL to the sphere with the same diameter, $\frac{2}{3}d$. The basic principle of using these instruments to simulate microscopic volumes is Fano's theorem (Fano 1954):

In a medium of given composition exposed to a uniform flux of primary radiation (such as X-rays of neutrons) the flux of secondary radiation is also

uniform and independent of the density of the medium as well as of the density variations from point to point.

But this is hard to fulfill because of polarization effects in solids. The shortcomings of walled detectors encouraged the study of a wall-less proportional counter (Glass and Braby 1969). It can be constructed by using either field shaping electrodes or grid wall. The size of grid wall detector can be built as small as a cylindrical of 1mm height by 1mm diameter, simulating cellular sites as small as 10 nanometers (Rayadurgam 2005). However, the boundary of the detector with field shaping electrodes is not well defined, and the grid walled detector is not truly wall-less.

Although it may be possible to use wall-less detectors to simulate different size sites, it would be easier to use solid walled detectors. Solid walled detectors will be simulated in this study. A walled proportional counter is easier to build than a wall-less (grid walled) one. It has a more rugged structure and less noise is introduced by the vibration of the wall. The chamber containing the detector can be smaller. The Monte-Carlo simulation needs less CPU time to generate a uniform field for a walled detector. Therefore, wall effects are still affecting the simulation results in this study.

Wall effects are classified into four types (Fig. 2.4) (ICRU 1983; Kellerer 1971a):

1. Delta-ray effect: A charged particle enters the cavity together with one of its δ-rays (double event) (Fig. 2.4a). In the real case, the distance between them is large enough that only one of them can enter the actual site with uniform density. Kellerer (Kellerer 1971b; Kellerer 1971c) found in his theoretical estimation that delta-ray effect is most important for HZE particles and high energy electrons. For protons of energies above 5 MeV, the double events have frequency of 15% in 1 μm site size. We can predict that for HZE particles with the same velocity this frequency could be much larger. Meanwhile, the effect on y_D is much less than that on y_F. That is because a HZE particle normally deposits much more energy than its δ-ray does. The major fraction of the dose is still due to the HZE particle.

2. Re-entry effect: An electron may re-enter a cavity after it has traversed it due to its winding backwards path (Fig. 2.4b). The points of exit and re-entrance may be too far apart for the electron re-enter the site with uniform density. This is only applied to electrons because their tracks are more tortuous than other heavy charged particles.

3. V-effect: Two or more charged particles produced in a non-elastic nuclear interaction enter the cavity together. The geometry in this effect is similar to delta-ray effect.

4. Scattering effect: An uncharged primary particle can produce two charged particles which are close enough apart to enter the cavity together. In the real case, their tracks may be far enough that only one of them can enter the actual site with uniform density. This effect is relevant to photons and neutrons.
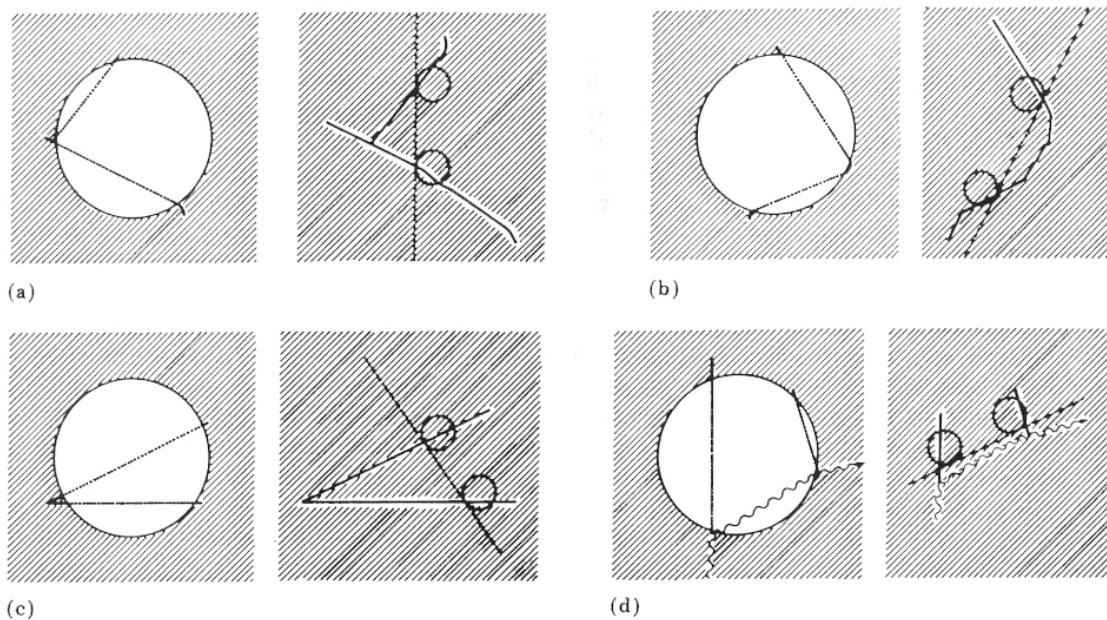
Fig. 2.4. Diagrams of the four types of wall effects. (a) delta-ray effect, (b)re-entry effect, (c) V effect, and (d) scattering effect (Fig. 5.1 of ICRU 1983).

In our study, the delta-ray effect is the most significant effect of the wall because HZE particle may generate a large number of δ-rays in a short track segment. The primary particle may enter the cavity with multiple electrons. At the same time, two or more δ-rays produced by one primary particle, which does not traverse the cavity, may enter the cavity together. The situation is similar to scattering effect. Since the effect on y_D is less than that on y_F, we can employ the $yd(y)$ vs $\log(y)$ plot instead of $yf(y)$ vs $\log(y)$ to get the absolute value of y_D. On the other hand, we want to use $yf(y)$ vs $\log(y)$ plot to illustrate the size effect because it shows more changes of y_F from different site size (see Chapter IV).

Radiation Weighting Factor

The radiation weighting factor, w_R, was once called qualitgy factor, Q. The equivalent dose in tissue T is

$$H_T = \sum_R w_R \cdot D_{T.R} \qquad (2.16)$$

where $D_{T.R}$ is the absorbed dose averaged over the tissue or organ T, due to radiation R. The specified values of w_R can be found in Table 1 of ICRP report 60 (ICRP 1991). To estimate the quality factor from the result of measurement or simulation, the relationship between quality factor and linear energy transfer may be more helpful (Annex A of ICRP 1991).

$$Q(L) = \begin{cases} 1 & L \leq 10\text{keV} / \mu\text{m} \\ 0.32L\text{-}2.2 & 10 \leq L \leq 100 \text{ keV} / \mu\text{m} \\ 300L^{1/2} & L > 100\text{keV} / \mu\text{m} \end{cases} \qquad (2.17)$$

where L is unrestricted linear energy transfer in water. Then the effective dose can be given by the expression

$$H = \int_0^\infty Q(L)D(L)dL \qquad (2.18)$$

where $D(L)$ is the dose distribution as a function of LET. If we have condition $y \approx L$, then equation 2.18 becomes

$$H \approx \int_0^\infty Q(y)D(y)dy \tag{2.19}$$

It should be noted that it is only a useful tool to get an estimate of H. According to the discussion in *Size Effect*, we know that equation 2.19 does not valid all the time. We should be careful to use it when dealing with spectrum measured in the same field by detectors with different size.

Cosmic Ray

Space radiations have three main categories according to their source (NCRP 1989): (1) trapped particle radiation, (2) galactic cosmic radiation (GCR) and (3) solar particle radiation. The majority of the fluence is protons, helium ions and heavier ions, with electrons and positrons making up a small fraction of the charged particles, as well as X-rays and γ-rays, which normally have comparably low energy. Neutrons will also be involved because of interactions of primary particles and shielding materials. Other subatomic particles, such as muons and pions, will also be generated but are not taken into account for dose evaluation because of very low population and very short half-lives (Clay and Dawson 1997).

As mentioned before, for each different kind of radiation, the biological effectiveness will be different. HZE particles are more damaging to cells than protons. Although the fluence of protons in galactic cosmic ray is about 7 times larger than that of helium ions, and is about 87 times larger than all of other HZE particles (NCRP 1989), the equivalent dose due to protons is about the same to or smaller than that of many HZE particles, including oxygen, silicon, and iron (Mewaldt et al. 2005; NCRP 1989). However, the traditional low pressure proportional counters mentioned above can not tell one particle from another, if they deposit the same amount of energy in the detector. This could happen to two particles, say an α particle and an oxygen ion from cosmic ray, with different charge and velocity. Evidently, they may have the same LET but different biological effectiveness. This is an obvious disadvantage for evaluation of the radiation quality and equivalent dose based on LET. Moreover, the shielding characteristics of materials vary for different radiations. The shielding in the spacecraft for electrons,

neutrons and ions requires different physical and engineering design. So, besides measuring the energy deposited and the stopping power of the particles, it is essential to characterize the radiation.
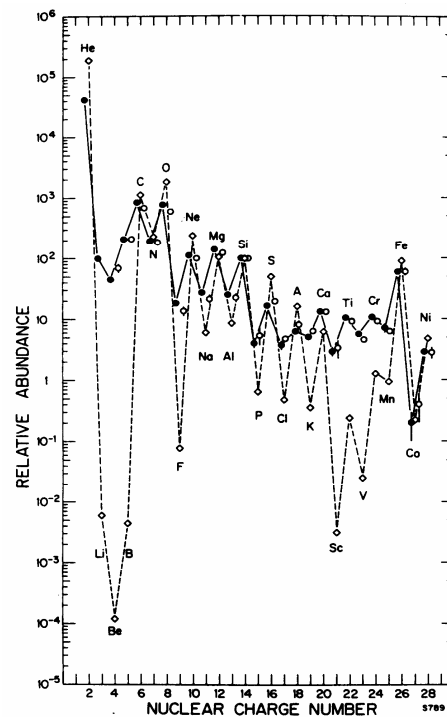
Fig. 2.5. The measured abundances of the elements relative to silicon ($\equiv 100$) in the galactic cosmic radiation (●-------● and open circles) compared to the solar system abundance (◇-------◇) (NCRP 1989).

The measured abundances of the elements relative to silicon ($\equiv 100$) in the galactic cosmic radiations and the solar system are shown in Fig. 2.5 (NCRP 1989). A wider spectrum of galactic cosmic ray can be found in Fig. 3.6 of NCRP (*National Council on Radiation Protection and Measurements*) Report No. 132 (NCRP 2000). Although it gives only the nuclear composition of galactic cosmic ray with energy ~2 GeV/n, it is still a typical composition in other energy range according to Fig 3.7 in NCRP 2000.

It is noticeable that other than the most abundant proton and helium, C, O, Si, Fe and other elements with even atomic number have larger abundance than those with odd
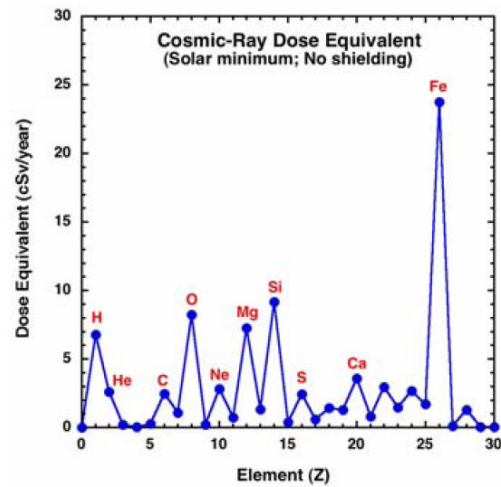
Fig. 2.6. Calculated contribution to the yearly equivalent dose (in cSv/yr) due to elements from H to Ni (assuming no shielding). Note that heavy elements make the largest contributions (Mewaldt et al. 2005).
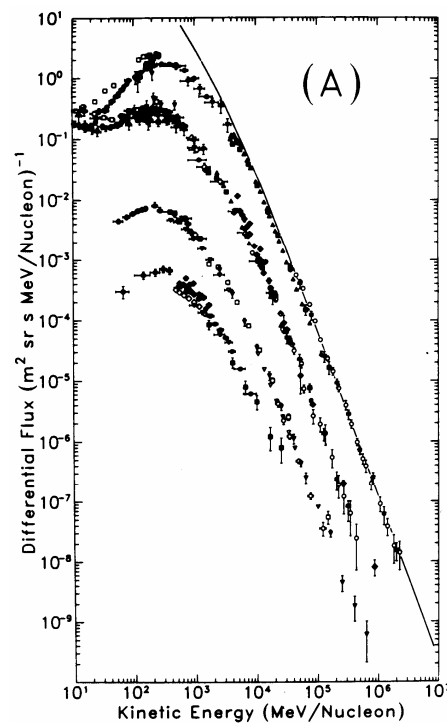
Fig. 2.7. Energy spectra of galactic protons, helium ions, carbon ions, and iron ions respectively (from top to bottom) at solar minimum (NCRP 1989).

atomic number near to them. A preliminary calculation shows that H, O, Mg, Si and Fe contribute most to the yearly equivalent dose (Fig. 2.6).

In Fig. 2.7, we can see the kinetic energy of galactic ions have most probable energy range from 100 to 1000 MeV/nucleon (NCRP 1989). The simulation will consists of series of calculation using different energies in this range.

Monte Carlo Toolkit

GEANT4 is the successor of GEANT3, the world-standard toolkit for HEP (high energy physics) detector simulation. The GEANT4 project started in Dec. 1994. The first GEANT4 public release was available in Dec. 1998. The versions released during this study is GEANT4 6.0 to GEANT4 8.0.p01.

GEANT4 (for GEometry ANd Tracking) is a platform for "the simulation of the passage of particles through matter" [1]. It is the most recent in the GEANT series of software toolkits developed by CERN and its collaborators, and the first to use Object oriented programming (in C++) [2]. "Its areas of application include high energy, nuclear and accelerator physics, as well as studies in medical and space science." [1]

Comparing with MCNP-5, which can be used for neutron, photon, electron, or coupled neutron-photon-electron transport, GEANT4 has taken into account a variety of requirements on heavy ion physics, CP violation physics, cosmic ray physics, astrophysics, space science and medical applications. It is capable of simulating more variety of particles and physics processes, including electromagnetic processes, hadronic processes photon / lepton - hadron processes and so on (Agostinelli et al. 2003; Allison et al. 2006). These processes are of great importance when simulation is required to produce accurate dose distributions for HZE particles passing through matter because of the various secondary radiations.

GEANT4 provides sets of alternative physics models so that the user can freely choose appropriate models according to the type of his/her application. In other words,

---

[1] Homepage of GEANT4: http://geant4.web.cern.ch/geant4/.

[2] From Wikipedia: http://en.wikipedia.org/wiki/GEANT4.

users of GEANT4 toolkit are responsible to select their own physics processes / models that are relevant to the simulation. The process selection is based on the physics object simulated, particle and energy range involved, simulation accuracy required, as well as experimental data library available. Each cross-section table or physics model has its own applicable energy range. One physics process can be applied over a wider energy range by combining more than one table and/or model. It should be noticed that the simulation accuracy as well as the calculation time is influenced by different physics processes or combination. Some models are more accurate than others at a sacrifice of speed. For instance, in this study, electromagnetic (EM) process in low energy range is of great interest because delta rays of low energy contribute a significant fraction of dose distribution. However, employing low energy EM (down to 250 eV) process boosts the demand for CPU time.

CHAPTER III

PROCEDURE

This chapter introduces the processes in determining the final conditions of simulation. The conditions include the geometry and material of detectors, mass and energy of incident particles, physics involved in the simulation and data recording.

Computer and Software

The simulations were performed on two servers (Table 3.1) in the Department of Nuclear Engineering, Texas A&M University, Texas. GEANT4 version 6.0 and 8.0.p01 were used in this study. Version 6.0 was used only to help determine the parameters in the simulation at the time when version 8.0.p01 was not available. The major calculation results were obtained using version 8.0.p01. The *Class Library for High Energy Physics* version used in simulations was CLHEP 1.9.2.2.a. The difference between the results obtained by two versions was studied and there was no observable difference given the simulation conditions used in this study. The related work will be introduced in *Physics Process*.

Table 3.1 The servers used in the simulation. The domain name is *ne.tamu.edu*.

Server Name	Server Type	Processor Specifications	Operating System	RAM
pine	Sun Fire V20z	2×AMD Opteron 248 (2.2 GHz)	Solaris 10	4GB
elm	Sun Fire V20z	2×AMD Opteron 250 (2.4 GHz)	Solaris 10	4GB

Detector

The most commonly used TEPCs are constructed either cylindrical or spherical. Cylindrical detectors have simple design in both structure construction and electric field

(Braby et al. 1995). According to Equ. 2.2, a cylindrical detector with height (*h*) same as its diameter (*d*) has a mean cord length of $\frac{2}{3}d$, which is identical to a sphere with the same diameter. When using in an isotropic field, such a cylindrical detector simulates as the spherical detector with the same diameter. But a cylindrical detector's response is not exactly isotropic. For example, the maximum chord length in the cylinder is 1.414*d* while it is *d* in the sphere. Practically, detectors are not always used in an isotropic field, when considering the surrounding shielding and the earth's magnetic field. So, spherical detectors are preferred for many situations.

Although there are some difficulties in constructing a spherical detector, simulating one in GEANT4 does not have to face the same problems. In a real detector, the end of anode is much closer to the wall, the electric field becomes stronger, thus the gas gain is higher. And the particles passing along very close to the anode within the avalanche area have different gas gain with those passing through from outside. In the Monte-Carlo simulation, energy deposition is collected in a class named *sensitive detector*. The anode and electric field are not applied in the simulated detector. Thus the difference of gas gain at different part of the detector is not considered. A uniform, parallel beam can be used to simulate the isotropic field when measuring with a spherical detector.

To build a tissue equivalent proportional counter, tissue substitutes are needed for the materials in the wall and the gas in cavity. It is not necessary to use material having the same component with tissue. But it is important for the material to have the same mass density and the similar radiation characteristics. In our study, the materials are required to have the same stopping power, and HZE particles and δ-rays can deposit approximately the same energy when going through same mass density thickness.

According to Bethe-Bloch formula(Attix 1986):

$$(\frac{dT}{\rho dx})_c = 0.3071\frac{Zz^2}{A\beta^2}[13.8373 + \ln(\frac{\beta^2}{1-\beta^2}) - \beta^2 - \ln I] \qquad (3.1)$$

stopping power is proportional to Z/A, which is the number of electrons per unit mass of the medium. It is proximately a constant for most low Z (<Ni) elements. The ln*I* (*I* is the *mean excitation potential* of the struck atom) in the bracket decreases the stopping power

as Z is increased. But for large β (high velocity of the primary particle with energy greater than 100 MeV/nucleon) and low Z material, this term has smaller effect on stopping power. In this study, we have more concerns on the magnitude of changes between measurements, than on the absolute value of each measurement. So we chose the most commonly used tissue equivalent materials. Water with unity density was used as the tissue equivalent wall material of the detector. Propane at pressure of 33 Torr (4.40 kPa) was used as the tissue equivalent gas in the cavity. Its density at standard temperature and pressure is 8.35×10^{-5} g/cm^3.

A preliminary Monte Carlo simulation was employed to determine the detector sizes. Four wall-less spherical proportional counters simulating tissue with diameter of 0.01, 0.1, 1, 10 μm were bombarded by uniformly distributed $^{56}Fe^{26+}$ particles which crossed the site. The detectors were housed in a vacuum chamber which was filled with propane at the same pressure. The delta rays that were produced outside of the detector have the possibility to enter the site, too. The chamber size changes according to the size of the detector. The nearest distance from the outside of the detector to each side of the chamber wall is 12.7 mm (0.5 inch). So the length of the rectangular vacuum chamber is 25.4 mm (1 inch) plus the diameter of the detector. This geometry design is to leave the same space around the detectors no mater what size they have. By doing so, time can be saved in simulation for small site size. To make it easier to distinguish the width, length and height of the chamber in a 3D-plot, the width was increased by 2 mm, and the length was increased by 4 mm. The particle distribution has obvious changes with the simulated site diameter (Figs. 3.1 and 3.2). The magnitude of change depends on the particle energy, because of the corresponding different delta ray range. The calculated mean lineal energy for 1000 MeV/nucleon iron particles which cross the site, y_F, decreases by 8.4% when the site diameter decreases from 10 to 1 μm and 4.0% when the site size decreases from 0.1 to 0.01 μm. The decrease of y_F for 100 MeV/nucleon ions is 9.8% when the site size decreases from 10 to 1 μm, and 5.7% from 0.1 to 0.01 μm.
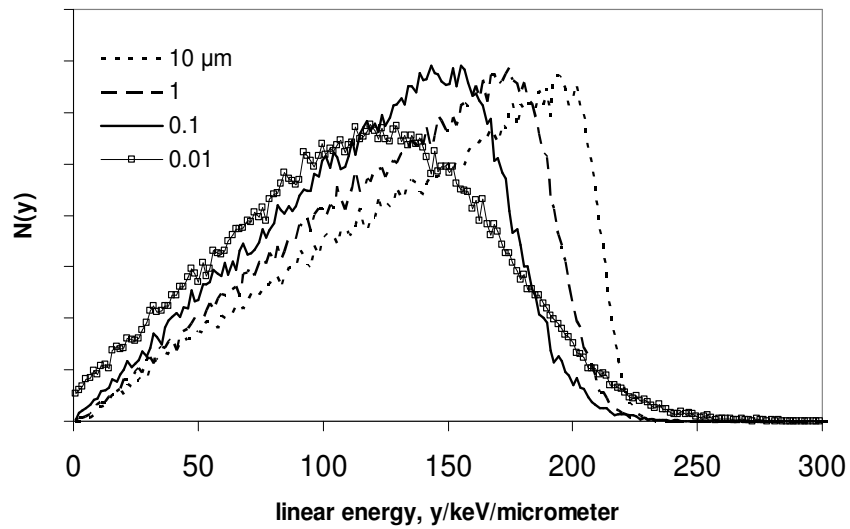
Fig. 3.1. Lineal energy distributions for 1000 MeV/n iron ions crossing different size sites. Energy imparted in the site, by the primary and its delta rays, estimated using GEANT4.
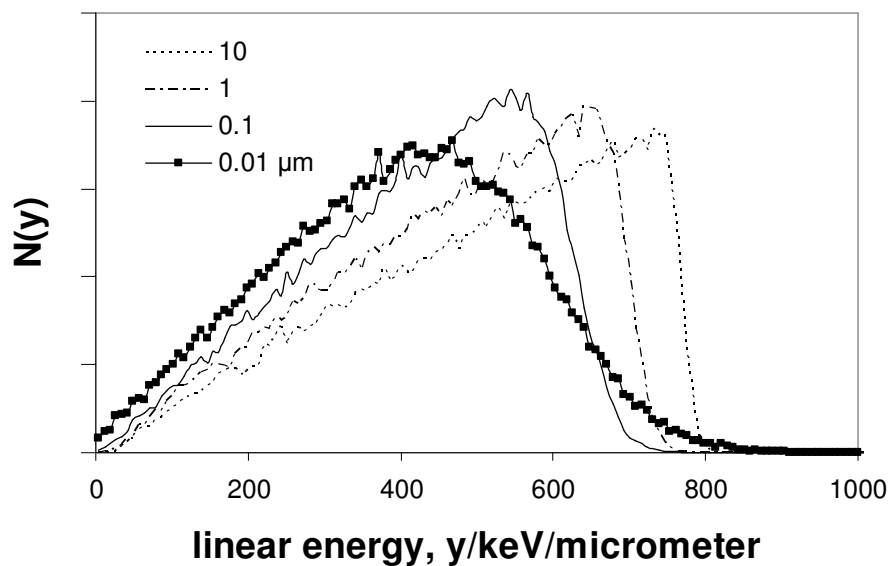

Fig. 3.2. Lineal energy distributions for 100 MeV/n iron ions crossing different size sites, simulated by proportional counter filled with propane. Same geometry was used as in Fig. 3.1.

Fig. 3.3 shows the preliminary simulation of four walled detectors, bombarded by 1000 MeV/nucleon $^{56}Fe^{26+}$. The simulated cavity sizes of detectors are 10, 1.0, 0.1 and 0.01 μm. The cavities were filled with propane gas at 33 Torr. The 'solid' wall is made of water with unity density and thickness of 1 mm. The detectors were housed in a low pressure chamber filled with 33 Torr propane. The beam diameter is equal to the outside diameter of the detector wall. Because the wall thickness is less than the maximum range of the most energetic δ-ray, the delta rays produced outside of the detector have the possibility to enter the site. Consequently, the vacuum chamber was made the same as that of wall-less detectors. The chamber size changes according to the size of the detector and there is same space between the detectors and the chamber wall for all detector diameters. Also, the width was increased by 2 mm, and the length was increased by 4 mm. This geometry design was used in the final simulations. The values of y_F are 162, 121 and 44.4 keV/μm for 10, 1 and 0.1 μm diameter sites, respectively. The effect of size on the shape of lineal energy distribution is apparent in this simulation.

The gas pressure is the same for all these detectors, thus the cavities' diameters decrease by factors of 10, from 127 to 0.127 mm (5 to 0.005 inch). For the smallest detector, the 0.127 mm diameter detector is embedded in a 2.127 mm diameter solid sphere. The solid angle of the detector is very small for the majority of the particle bombarding the solid wall. For each calculation, 10^5 particles were simulated. The relatively poor statistics obtained when simulating the 0.01 μm detector can be seen in Fig. 3.3. Such a small detector will also create problems in construction and measurement. Although we can use smaller gas pressure (density) to increase the cavity size for construction convenience, the single ionization events still constitute a large portion of the total number of measured events and the statistics of gas avalanche will result in a large variance in pulse height. For single ionization events with approximate 30 eV average energy imparted, the events have an average lineal energy 4.5 keV/μm in a 0.01 μm diameter site. In Fig. 3.3, we can see that the frequency of events smaller than 5 keV/μm plays a major role in determining the y_F for a 0.01 μm diameter site. Measurement of such small energy depositions involves large uncertainties. Further

more, the spectrum for a 0.01 μm site does not differ significantly from the spectrum for a 0.1 μm site, and the difference between the other three spectra is much more obvious. As a result, we did not use 0.01 μm site in the simulations.
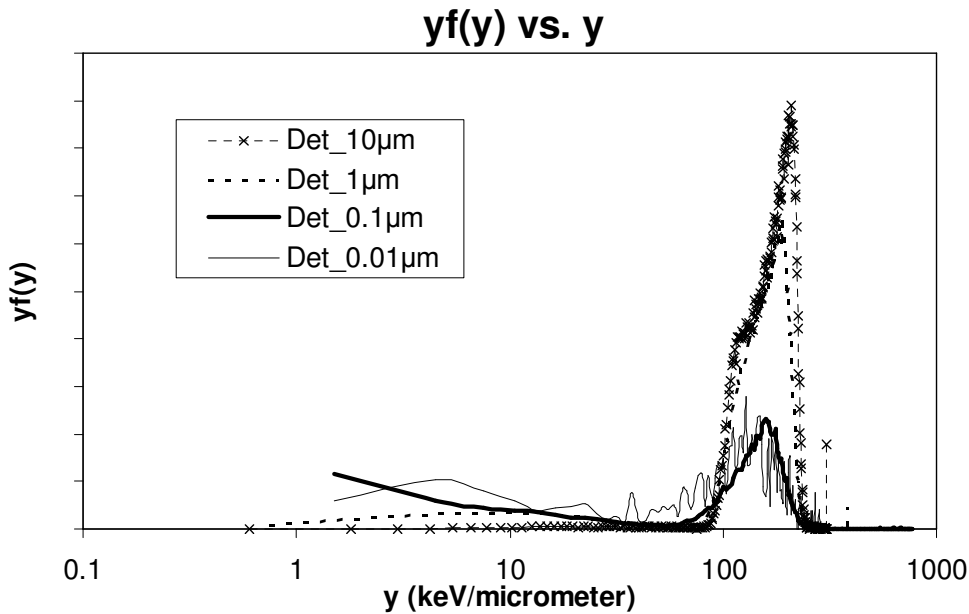
Fig. 3.3. Probability density, f(*y*), for a uniform broad beam of 1000 MeV/n iron ions irradiating solid walled (wall thickness 1 mm) detectors simulating sites 0.01, 0.1, 1, and 10 micrometers in diameter. The walled cavities were filled with propane gas at 33 Torr and housed in a low pressure chamber. The beam diameter is equal to the outside diameter of the wall.

On the other hand, the change of y_F value seems to become small when the detector diameter changes from 1 to 10 μm for 1 GeV/nucleon ions, which is the representative of much of the GCR spectrum. A smaller range of site sizes may be more proper to show the size effect. The diameter of the detectors in this study was chosen to be 2.5, 0.5 and 0.1 μm. For the purpose of this study the sites will be simulated by detector diameters of 31.75, 6.35 and 1.27 mm (1.25, 0.25 and 0.05 inch), respectively. The ratio of count rates to the count rate in the smallest site, in a uniform field, will be 625 and 25. The

moderate size and count ratio will bring much more convenience in detector assembly and measurement.

Particle Selection

The HZE ions used in this simulation will be a few nuclides with large abundance. Oxygen, silicon and iron are among the HZE particles with highest abundance in cosmic ray spectrum. As to the specific isotopes concerned in the calculation, nuclides with even-even proton-neutron number normally have the greatest abundance because of their superior stability (Kaplan 1956). In this work, fully stripped ions of ^{16}O, ^{28}Si, ^{56}Fe will be used as the primary particle, with ^{4}He and protons for comparison.

As discussed in Chapter II, these cosmic particles have a large energy distribution range. The most probable energy ranges from 100 to 1000 MeV/nucleon. For each simulation, a mono-energetic beam of one ion will be used. Each ion will be calculated with energy of 100, 500, and 1000 MeV/nucleon, respectively.

This simulation study is designed to be compared with an experimental study to be conducted seperately. The detectors will be irradiated by the beam generated by a synchrotron. These particles are available periodically at the NASA space radiation laboratory.

Wall Thickness

The same wall thickness will be applied on every detector simulated. This is based on the practical experiment considerations. Once the detectors are assembled, they can be used to measure any relavent the radiation field. Although the simulated site size can be adjusted after the assembly by changing the gas pressure, the thickness of the solid wall will be fixed.

Simulating a uniform field requires a lot more CPU time than just deliver a parallel beam of a certain diameter. Moreover, the detector has a very small solid angle to most of the particles in uniform fields. The whole simulation efficiency (effective counting rate) becomes even lower. To solve this problem, a beam was applied to cover just the

cross section of the spherical detector wall. If the wall is thick enough that no secondary electrons can penetrate, and its thickness is small enough compared to the HZE particle's range, such a simplification is equivalent to a uniform field.

The maximum energy that can be transferred to an atomic electron in a head-on collision is (Attix 1986):

$$T'_{max} \approx 2m_0 c^2 (\frac{\beta^2}{1-\beta^2}) = 1.022(\frac{\beta^2}{1-\beta^2}) MeV \qquad (3.2)$$

where m_0 is the rest mass of a electron, c is the speed of light in vacuum, $\beta = v/c$ and v is the velocity of the primary particle. Obviously, 1000 MeV/nucleon particles can generate more energetic δ-rays than 500 and 100 MeV/nucleon particles. If the wall can stop all the δ-rays generated outside by 1000 MeV/nucleon, the same wall thickness can be applied to 500 and 100 MeV/nucleon particles.

It should be mentioned that the wall has 1.2×10^4 times larger density than that of the 33 Torr propane gas. The interactions are much more intense in the wall and the increase of the wall thickness will result in dramatic increase calculation time. The wall thickness is one of the key values affecting the calculation time. This issue is most important for the heavy particles with low energy, because they can generate more δ-rays, which are the main consumer of CPU time.

According to Equ. 3.2, the maximum energy of δ-rays generated by an 1 GeV/nucleon $^{56}Fe^{26+}$ particle is about 3.38 MeV. That corresponds to a CSDA (continuous slowing down approximation) range of 1.77 cm in water. The maximum range of electrons can be larger than CSDA range because of the effect of range straggling. However, for low-Z media, the maximum range of electrons is comparable to CSDA range (Attix 1986). Even so, a wall of 1.77 cm is still unacceptable for simulations using available computers. More than 100 hours are needed to calculate 100,000 1 GeV/nuleon $^{56}Fe^{26+}$ particles when using only 4 mm thick wall. The calculation step length can be increased to decrease the amount of calculation of δ-rays. But this will certainly sacrifice the accuracy of result.

A condition that can fulfill the ideal simplification of a uniform field was also evaluated for the 500 MeV/nucleon iron particles. Their δ-rays have maximum energy of 0.55 MeV, corresponding to 0.2 cm CSDA range in water. This thickness requires reasonable calculation time when retaining good accuracy. Fig. 3.4 shows frequency distribution for an 1 μm simulated site with 1, 2, and 3 mm thick wall of water irradiated by a uniform 500 MeV/nucleon iron beam. The cavities were filled with propane gas at 33 Torr and the detectors were housed in a chamber filled with propane at 33 Torr. The beam diameter is equal to the outside diameter of the wall. The 2 mm result matches the 3 mm result very well. The y_F has a change of less 1%. While the 1 mm shows about 11% of increase of y_F. So, 2 mm wall was used for all the detectors in this study. It fulfills the uniform field simulations for 500 and 100 MeV/nucleon particles. Although the simulation of 1 GeV/nucleon particles uses the same wall thickness, further analysis is required to interpret the results.
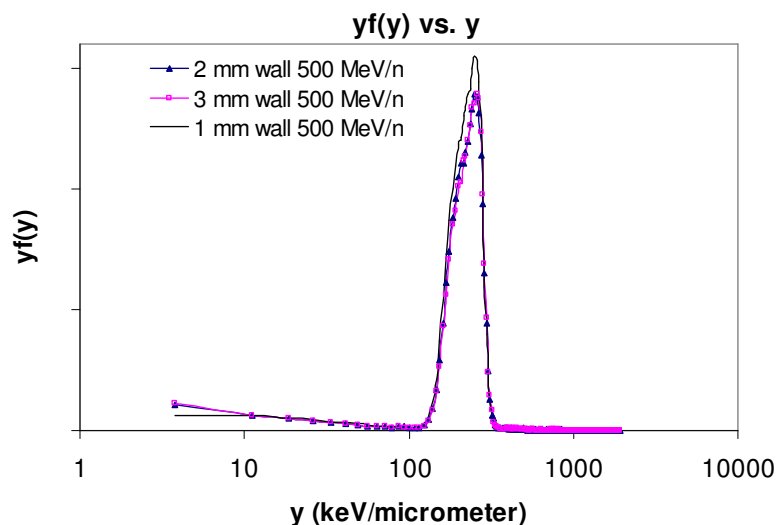
Fig. 3.4. Simulation results of different wall thickness. An 1 μm simulated site with 1, 2, and 3 mm thick solid wall was irradiated by a uniform 500 MeV/nucleon iron beam. The cavities were filled with propane gas at 33 Torr and the detectors were housed in a low pressure chamber. The beam diameter is equal to the outside diameter of the wall. The results of 2 mm and 3 mm wall thickness match each other very well.

Physics Processes

Selecting physics processes is of great importance in the simulations. GEANT4 gives users enough freedom to choose various particles and physics models according to their specific requirement. But it is also the user's responsibility to examine if the processes are properly chosen and / or combined, and if the processes provide a good balance between the accuracy and CPU time requirements. The particles and physics processes involved in this study will be discussed in this section.

There are seven major categories of processes provided by GEANT4:

1. electromagnetic,
2. hadronic,
3. decay,
4. photolepton-hadron,
5. optical,
6. parameterization and
7. transportation.

The first three processes are the major processes involved in the simulations. If the primary and secondary particles are unstable, decay process may happen after a step of transportation when the particle is 'at rest' (*AtRest* action). The decay process does not happen along the step because it will cause the change of particle, physics model and cross section data. Considering the primary particle used in this study are all stable nuclei and the cross section for nuclei-nuclei reaction is much lower than that of electromagnetic process, we don't adjust the parameters according to decay process. Hadronic process was included in the simulation. It is important when using proton and ^{4}He as primary particles. GEANT4 provides various examples for application to different fields. Users normally develop their application from one or more related examples. This simulation also starts from existing examples. The well developed code for the processes and related particles used in the simulations can be found in the extended analysis example of A01[1] in installation folder of GEANT4.

---

[1] This example can be found under installation folder of GEANT4: ../example/extended/analysis/A01/.

The electromagnetic (EM) process is of the greatest importance in those three processes. HZE primary particles and δ-rays deposit energy mainly by EM process. Positrons and photons are also defined for EM process. The *standard* EM processes provided by GEANT4 toolkit were used in this simulation. Four sub-processes are included, and each has its physics processes and related class names. Table 3.2 gives a summary of the standard EM processes. The synchrotron radiation was not registered in the simulations. For charged particles, the physics processes are performed along the step (*AlongStep* action) or after the step (*PostStep* action). The order to perform the processes is:

1. Multiple scattering,
2. Ionisation,
3. Bremsstrahlung (if applicable),
4. Annihilation (if applicable).

For photons, the processes are performed as PostStep actions. The order is:

1. Electric effect,
2. Compton scattering,
3. Gamma conversion.

But for processes which have only PostStep action, the ordering is not important.

GEANT4 also provides a series of low energy electromagnetic (LE EM) processes, which is included in version 6.0 and was further developed in 8.0.p01 and later versions. They are a set of processes extending the coverage of electromagnetic interactions down to lower energy. The lower limit is 250 eV (in principle even below this limit) for electrons and 100 eV for photons, while they are 1 keV in standard EM processes. For hadrons and ions, the energy is approximately down to the ionization potential of the interacting material. The upper limit of the energy can reach up to 100 GeV. All processes are based on theoretical models and on exploitation of evaluated data.

Theoretically, LE EM processes can give more accurate simulation results when low energy electrons and photons are involved. In our simulation, the low energy δ-rays are a large portion of the population. The accuracy of their distribution affects that of y_F and

y_D. However, this will boost the requirement of CPU time dramatically. Since we only trace a short range of the primary particle's track in the chamber, the energy of primary particle are still very high. For example, 1 GeV/nucleon ^{56}Fe particle's range in water is around 26.82 cm, and 1 GeV/nucleon ^{16}O can go through 80.94 cm. Within the range of the chamber and detectors, the HZE particles' energy retains almost the same value during the calculation. It is not important to use LE EM processes for the primary particle.

Table 3.2. Summary of standard EM processes.

Process name	Physics of the process	Class name
Photon processes	Compton scattering	G4ComptonScattering
	Gamma conversion (pair production)	G4GammaConversion
	Photo-electric effect	G4PhotoElecticEffect
Electron/positron processes	Bremsstrahlung	G4eBremsstrahlung
	Ionization and δ-ray production	G4eIonisatoin
	Positron annihilation	G4eplusAnnihilation
	The energy loss process	G4eEnergyLoss
	Synchrotron radiation	G4SynchrotronRadiation
Hadron processes	Ionization	G4hIonisation
	Energy loss	G4hEnergyLoss
The multiple scattering process	Multiple scattering of all the charged particles (e+, e-, muons and charged hardons)	G4MultipleScattering

But 10 keV electrons have a CSDA range of only 2.515 μm in water (Attix 1986). An electron with energy of 100 eV has a range of a few orders of magnitude shorter. The step length in GEANT4 was defined by *Cut Value*. It is the thickness of the thinnest

media layer for each calculation step. If a δ-ray can not go through such a layer of media, it will not be emitted. Its energy is taken as depositing locally. Generating such a low energy electron means using very small cut value and tracing enormous numbers of electrons down to very low energy. According to the power of the server pine and elm, we finally chose a cut value of 0.01 mm. It is certainly much larger than the range of a 1 keV electron.

The primary particle which is going through the site deposits energy together with peripheral δ-rays. It is recognized by the detector as one *primary event*. The event produced by the δ-rays which are raised by a primary particle in the wall is one *δ-ray event*. If a δ-ray's energy is below the energy threshold related to the cut value and it does not come into being in the simulations, its energy will be taken as deposited locally, by the primary particle. So the energy deposited by a primary event should be the same using different cut value (omitting the influence of the media boundary).

However, these 'virtual' δ-rays can be as low as 250 eV in LE EM processes, whereas they are 1 keV in standard EM processes. The LE EM processes will still slow down the calculation by judging whether or not to emit a low energy δ-ray. So, standard EM processes were used in the simulations. Fig. 3.5 shows the difference between the results with these two sets of EM processes. A 500 MeV/nucleon $^{56}Fe^{26+}$ uniform beam was used with 1 μm site with 2 mm wall. The diameter of beam equals that of the detector wall. The cut value in these simulations is 0.001 mm. The y_F are 158 and 134 keV/μm for low energy and standard EM processes, respectively. There is about 15% decrease of y_F when using standard EM processes. The results are 155 and 133 keV/μm, respectively, when the cut value is 0.01 mm, corresponding to 14% decrease. Since adopting less accurate physics processes and step length will affect all the calculations by the same mechanism, the Size Effect should be simulated with reasonable accuracy using the 0.01 mm cut value and standard EM processes.

Cut value determines how many δ-rays generated at the very boarder (last step) of wall and gas cavity can go into the adjacent media. For δ-rays going into the cavity from the wall, the 0.01 mm cut value affects the energy deposition by only about 0.5% (0.01

mm / 2 mm) of the events. For δ-rays going out from the cavity into the wall, the influence becomes much smaller because the same step length in propane corresponds to much lower energy range. It prevents fewer δ-rays from going outside than the same layer of water does. Fig. 3.6 shows the difference between results by using 0.001 and 0.01 mm cut value. The y_F is 134 and 133 keV/μm, respectively. The difference is only about 1%.

It should be noticed that in both processes the calculations employ the condensed history method for the electron tracks. That means the tracks are simulated using the continuous slowing down approximation. They neglect the energy loss straggling when calculate the energy deposited. This approximation will affect the variance of the calculated energy deposition and the corresponding mean lineal energy. However, they still provide a good estimate of the number of δ-rays reaching and leaving the site. The impact of this approximation on accuracy was not studied in the work because it was not a primary concern for this application.
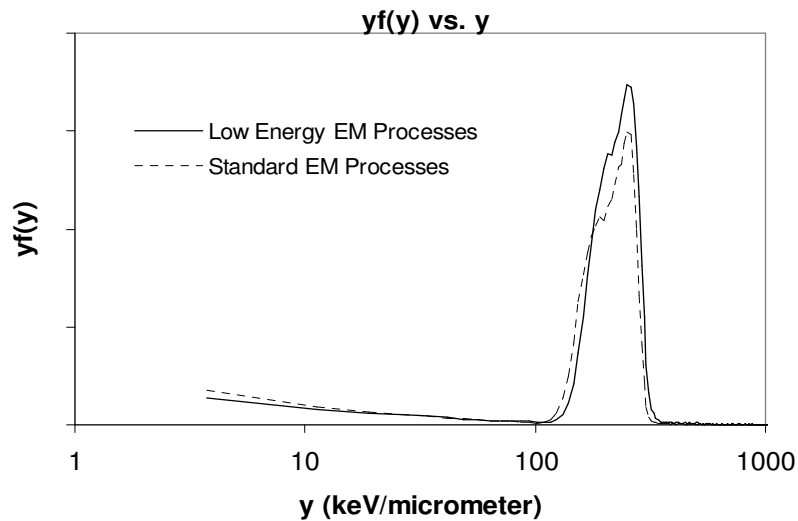
Fig. 3.5. Lineal energy distribution of a 500 MeV/nucleon $^{56}Fe^{26+}$ uniform beam in 1 μm site with 2 mm wall with different EM processes. The diameter of beam equals that of the detector wall. The cut value in these simulations is 0.001 mm.
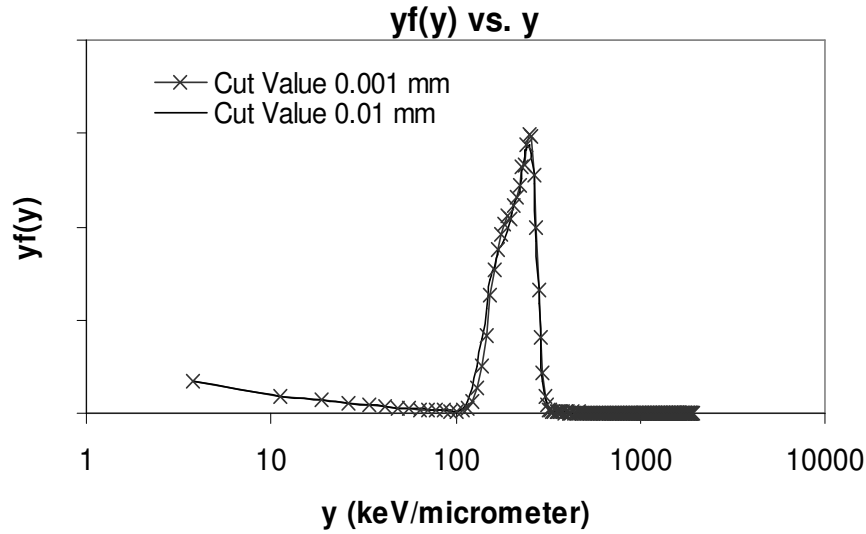
Fig. 3.6. Lineal energy distribution of a 500 MeV/nucleon $^{56}Fe^{26+}$ uniform beam in 1 μm site with 2 mm wall with different cut value. The diameter of beam equals that of the detector wall. The cut values in these simulations are 0.001 and 0.01 mm. Standard EM processes were used in the calculations.

Data Recording

The number of events (counts) is normally recorded in the corresponding channel according to the energy deposition of the event. Because data will be collected from different sites, events that have same energy may not have same lineal energy. Note that the abscissa of the distribution plot is lineal energy *y*. In order to make it easier to compare the data from different simulations, counts were recorded according to lineal energy. A total of 256 channels were used for the whole spectrum. The width of a channel is d (keV/μm). So, the whole spectrum covers the range from 0 to 256d keV/μm. The event with lineal energy $N \cdot d \leq y < (N+1) \cdot d$, $(N \geq 0)$ will produce one count in the Nth channel. All the events with energy equal or larger than 256d keV/μm will be taken as events in the 255th channel.

There is another reason to use lineal energy rather than energy as the channel width unit. As mentioned in Chapter II, the start point of a semi-log plot changes the

appearance of curve normalization. A good example is Fig. 3.3. The curves start from different *y* values. Intuitively, the area under 0.1 μm detector is smaller than that under 10 and 1 μm detectors. The linear channel width in a linear axis becomes non-linear in a logarithmic axis. Although the data were normalized for each curve, the beginning point of the histogram makes big difference. Using energy as the channel width unit to record the data will cause different start point of *y* for different site size. While using lineal energy as the channel width unit brings much convenience into comparison.

Even so, the curve of 0.1 μm detector in Fig. 3.3 has another deficiency. The first channel has a large count. It includes all the low energy events in one channel. The information of distribution below the start point was lost. It can be easily solved if smaller channel width and more channels are used. But this will cause another complexity. The statistic in each channel becomes low and the data becomes too sparse at the high lineal energy range. The calculation time will increase if a larger number of particles are calculated to get better statistics.

An alternative method is recording the data simultaneously twice by using two channel widths. In experiments, it is realized by using two amplifier gain values. The data using smaller channel width (high amplifier gain value) shows the low energy portion of the spectrum. Meanwhile, the data using large channel width covers all the energy range and shows the high energy portion better. Combining the two sets of data at a certain point can give a whole spectrum containing details in both ends. In this study, channel width of 0.1 keV/μm and 5 keV/μm was used for HZE particles and ^{4}He. Only 256 channels were used for each gain. The spectra were *welded* at the 199th and 4th channel of the small and high channel width, respectively. The *welding point* energy was 30 keV/μm. Channel width of 0.02 keV/μm and 1 keV/μm was used for protons. The spectra were welded at the same channels. The welding point was 6 keV/μm. The welded spectra are used in Chapter IV. This approach not only shows better details at low lineal energy, but it also provides better normalization.

CHAPTER IV

RESULTS AND DISCUSSION

In this chapter, we discuss the results of the simulations. The calculations were performed for $^{56}Fe^{26+}$, $^{28}Si^{14+}$, $^{16}O^{8+}$, $^{4}He^{2+}$ and proton. The energy used was 1000, 500, and 100 MeV/nucleon for each particle. 100,000 particles were used in each calculation. The beam diameter was equal to the outside diameter of the detector wall. The diameters of the simulated sites were 2.5, 0.5 and 0.1 μm. The detectors have 2 mm wall made of water with unit density. The cavities and chambers were filled with 33 Torr propane gas. The chamber's size changed with the detectors' size. The detailed geometry can be found in Chapter III. Standard EM processes were employed in the simulations discussed in this chapter. Cut value was 0.01 mm for all calculations. The method of welding spectra was applied to draw the plots.

Illustration

The 500 MeV/nucleon $^{56}Fe^{26+}$ was chosen as a stereotype of this study. They make up a significant fraction of the GCR spectrum (Fig. 2.5) and the largest contribution to equivalent dose (Fig. 2.6). Due to its large charge, the iron particle generates more δ-rays than the lighter nuclei. The geometry of the detectors is ideal for particles with energy of 500 MeV/nucleon and lower. The δ-rays of a 500 MeV/nucleon iron are more energetic than those of 100 MeV/nucleon particles. The size effect is expected to be more distinct for 500 MeV/nucleon $^{56}Fe^{26+}$ particles.

Fig. 4.1 shows the frequency distribution of 500 MeV/nucleon $^{56}Fe^{26+}$ particles in different size sites. The difference between each simulation is distinct. The frequency mean, y_F is 177, 91.5 and 25.3 keV/μm for 2.5, 0.5 and 0.1 μm site size, respectively. The peak at the high lineal energy end is composed of energy deposition of both the primary particle and δ-rays. There is a slight left shift of the peak with decrease of the size. That is because the δ-rays have more chances to escape from a smaller size site. The HZE particle's stopping power does not change much in the site and deposits most

of energy for the events of the peak. But the δ-rays' change much more in the short range and cause a small amount of change of y_F. The low lineal energy portion of the curves is composed of δ-ray events only. The probability of δ-ray events increases as the site size decreases. It is because the change of site size alters the cross section ratio of the cavity to the whole detector. For 0.1 μm site size, the cavity used in the simulation is 1.27 mm in diameter. The thickness of the wall is 2 mm. Since the beam was uniformly distributed within the diameter of the wall, the possibility of the cavity being hit directly by the primary particle is smaller than that of the wall. And the bombardment in the wall can only generate δ-ray events in the site.
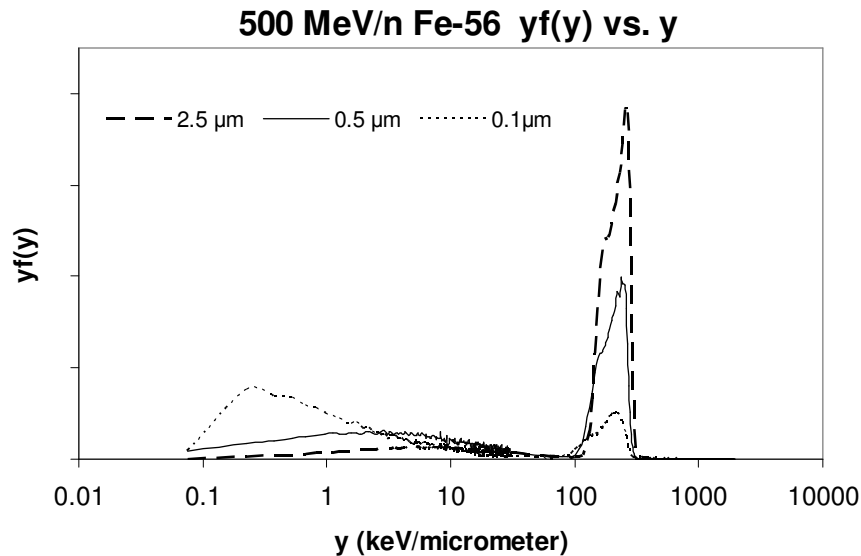
Fig. 4.1. The frequency distribution, $yf(y)$, for a uniform broad beam of 500 MeV/nucleon iron ions irradiating solid walled detectors simulating sites 2.5, 0.5, and 0.1 μm in diameter.

Fig. 4.2 shows the dose distribution of 500 MeV/nucleon $^{56}Fe^{26+}$ particles in different size sites. The dose mean y_D is 225, 205 and 181 keV/μm for 2.5, 0.5 and 0.1 μm site size, respectively. The difference is not as prominent as that in $yf(y)$ vs. y plot. The peak still shift left with the site size decreases. But it is noticeable that the portion of

dose of δ-ray events is small and does not change much with the size. That is because the energy deposition of the primary particle is much larger than δ-rays. Even the probability of δ-ray event increases in smaller sites, the dose delivered by them is still a small portion of the total.

Comparing Figs. 4.1 and 4.2, we will take the advantage of $yf(y)$ vs. y plot to illustrate the size effect.
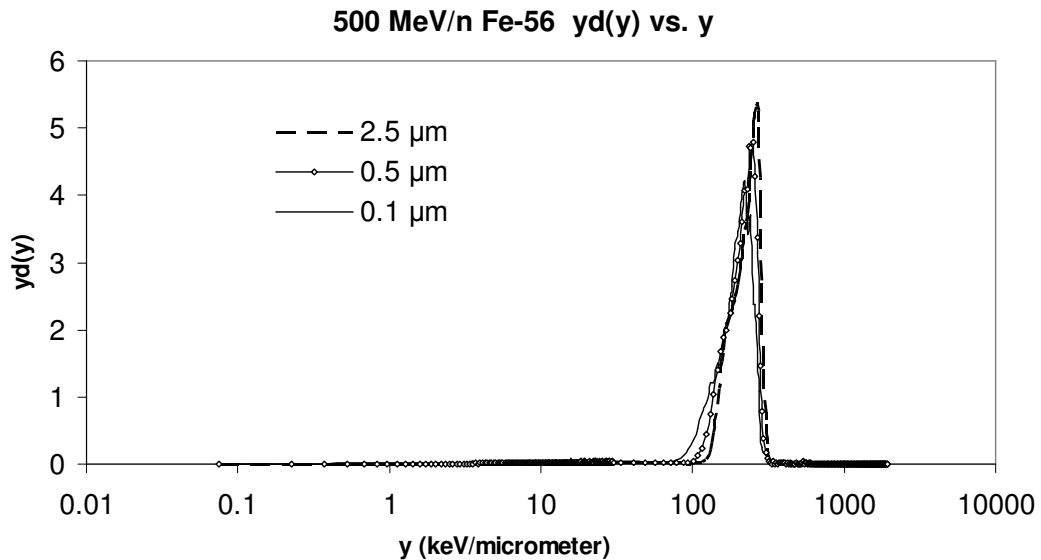
Fig. 4.2. The dose distribution, $yd(y)$, for a uniform broad beam of 500 MeV/nucleon iron ions irradiating solid walled detectors simulating sites 2.5, 0.5, and 0.1 μm in diameter.

500 MeV/nucleon Particles

The simulation results of 500 MeV/nucleon particles will be discussed in this section. Fig. 4.3 shows the frequency distribution of 500 MeV/nucleon $^{28}Si^{14+}$ particles in different size sites. The frequency mean are 52.2, 31.0 and 11.7 keV/μm for 2.5, 0.5 and 0.1 μm site size, respectively. Fig. 4.4 shows the frequency distribution of 500 MeV/nucleon $^{16}O^{8+}$ particles in different size sites. The frequency mean are 17.7, 12.3 and 6.36 keV/μm for 2.5, 0.5 and 0.1 μm site size, respectively. Fig. 4.5 shows the frequency distribution of 500 MeV/nucleon $^{4}He^{2+}$ particles in different size sites. The

frequency mean are 1.23, 1.11 and 1.00 keV/μm for 2.5, 0.5 and 0.1 μm site size, respectively. Fig. 4.6 shows the frequency distribution of 500 MeV protons in different size sites. The difference between each size site is distinct. The frequency mean are 0.339, 0.344 and 0.279 keV/μm for 2.5, 0.5 and 0.1 μm site size, respectively. These spectra can be easily distinguished from each other, even by using one detector.

For each particle, the size effect is prominent. The results from different size site can be distinguished from each other from both the lineal energy distribution and the calculated y_F. Table 4.1 is the summary of y_F and the ratio of y_F between different site sizes irradiated by 500 MeV/n particles. The y_F of 2.5 μm site was taken as 100%. The y_F decreases much faster with the site size for high Z particle than low Z ones. It is because high Z particles have larger stopping power and generate many more δ-rays than low Z ones. The different escaping rate of δ-rays causes the size effect. The more δ-rays being generated, the more variation occurs when the site size changes.
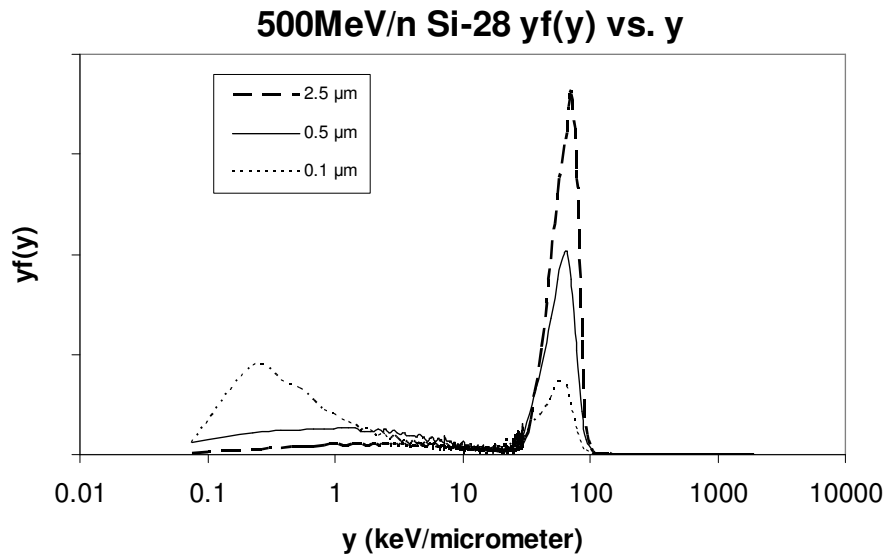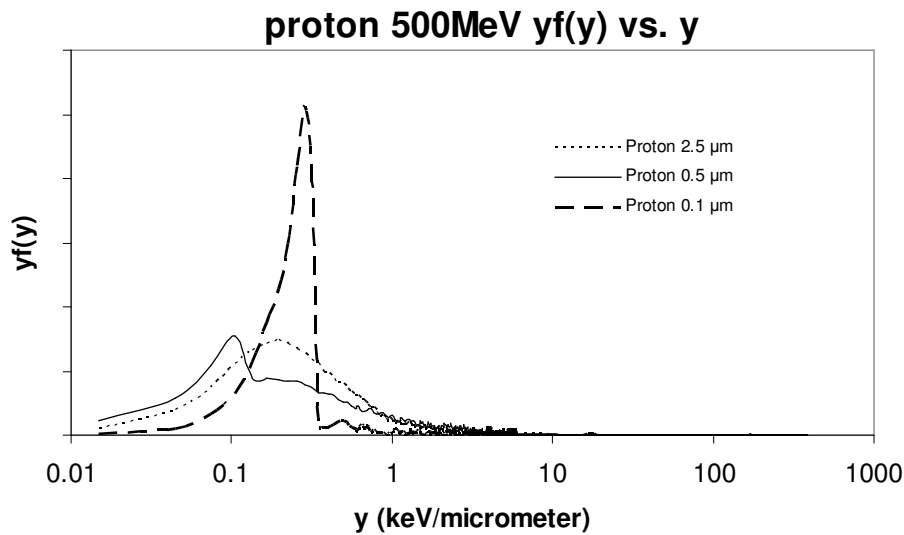

Fig. 4.3. The frequency distribution, $yf(y)$, for a uniform broad beam of 500 MeV/nucleon $^{28}Si^{14+}$ irradiating solid walled detectors simulating sites 2.5, 0.5, and 0.1 μm in diameter.
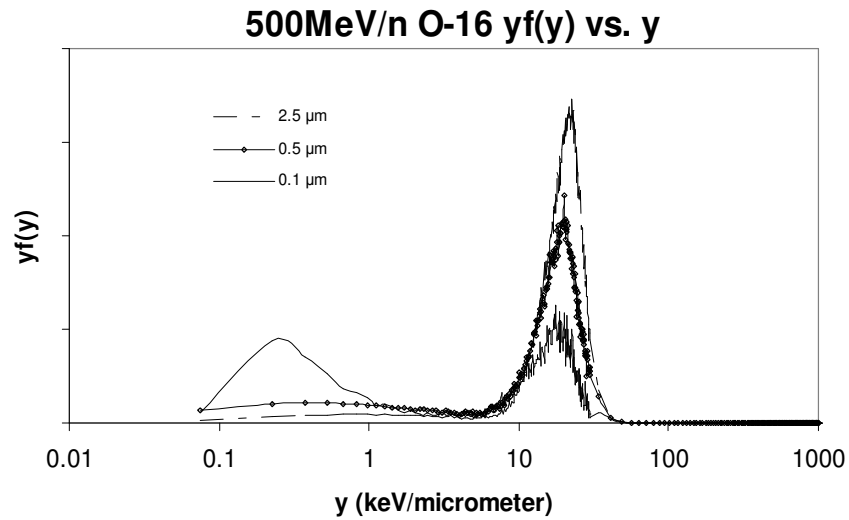
Fig. 4.4. The frequency distribution, $yf(y)$, for a uniform broad beam of 500 MeV/nucleon $^{16}O^{8+}$ irradiating solid walled detectors simulating sites 2.5, 0.5, and 0.1 μm in diameter.
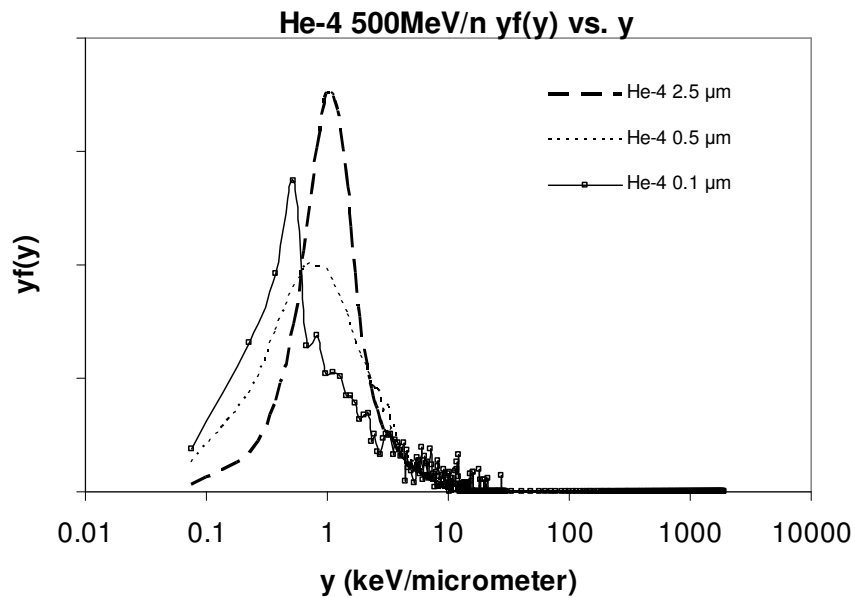
Fig. 4.5. The frequency distribution, $yf(y)$, for a uniform broad beam of 500 MeV/nucleon $^{4}He^{2+}$ irradiating solid walled detectors simulating sites 2.5, 0.5, and 0.1 μm in diameter.

proton 500MeV yf(y) vs. y

Fig. 4.6. The frequency distribution, $yf(y)$, for a uniform broad beam of 500 MeV proton irradiating solid walled detectors simulating sites 2.5, 0.5, and 0.1 μm in diameter.

Within the same size, the y_F is larger for particles with higher Z. Iron has the largest y_F among those simulated particles. It is because the increasing stopping power, including ionization and excitation ability of the primary particle, and the corresponding increasing number of δ-rays. For large site size, the primary particles contribute most to the y_F. The Fig. 4.7 shows the relationship between the charge and the y_F for each site size. Since most of the events in 2.5 μm site are the primary events, its y_F is most likely to be proportional to Z^2, where Z is the charge of the primary particle. In smaller sites, the contribution of δ-rays increases, so the results will deviate from the Z^2 relationship. The fitting curve shows this tendency.

All the above properties of the simulated results show that there are obvious changes of the spectra with both site size and charges of primary particles, for mono-energetic particles. This detector system can not only provide information of the dose but also the information of the incident particles within a small energy range. In the following section, we will discuss the simulation results with different energy.

Table 4.1. The summary of y_F and the ratio of y_F between different site sizes irradiated by 500 MeV/n particles. The y_F of 2.5 µm site was taken as 100%.

Particles	Site Size	2.5 µm	0.5 µm	0.1 µm
$^{56}Fe^{28+}$	y_F	177	91.8	25.3
	ratio	100%	51.9%	14.3%
$^{28}Si^{14+}$	y_F	52.2	31.0	11.7
	ratio	100%	59.4%	22.4%
$^{16}O^{8+}$	y_F	17.7	12.3	6.36
	ratio	100%	69.5%	35.9%
$^{4}He^{2+}$	y_F	1.23	1.11	1.00
	ratio	100%	90.2%	81.3%
proton	y_F	0.339	0.344	0.279
	ratio	100%	101%	82.3%
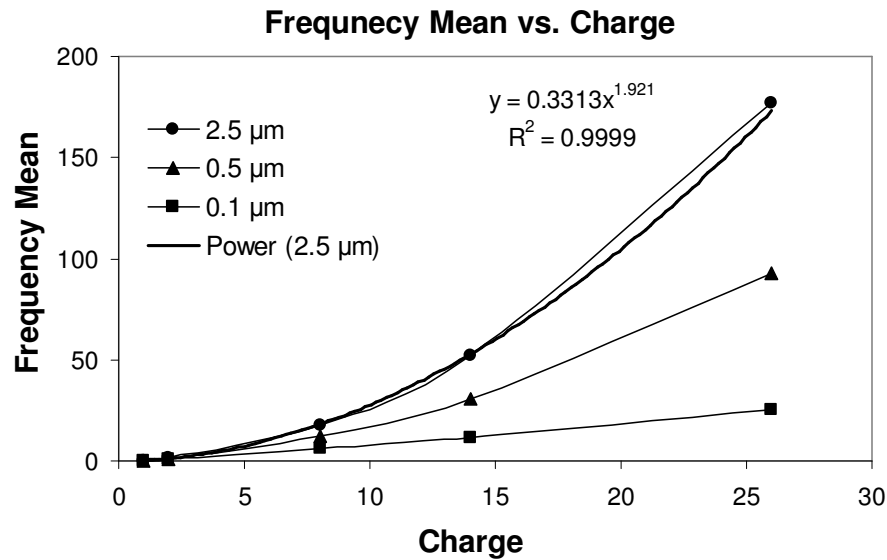
Fig. 4.7. The relationship between charge and y_F for each site irradiated by 500 MeV/n particles. The dark line and equation is the fitting curve for 2.5 µm site size. The power of the fitting equation is close to 2.

Energy Change

The size effect for particles with different energy is of great importance for unserstanding the system's response to a complicated filed. Fig. 4.8 shows the frequency distribution of 100 MeV/nucleon $^{56}Fe^{26+}$ particles in different size sites. The frequency mean are 737, 610 and 375 keV/μm for 2.5, 0.5 and 0.1 μm site size, respectively. These values are much larger than the 177, 92.5 and 25.3 keV/μm for 500 MeV/nucleon iron particles. It is due to the larger stopping power (494.3 keV/μm in liquid water) of iron particle with smaller velocity or value of β. Furthermore, for the events of the peak, the primary particles and low energy δ-rays contribute much larger portion of the total energy deposited. They play a dominant role in this situation even though the production of high energy δ-rays is high. So, when the size changes, the escaping δ-rays do not make as much change as for 500 MeV/nucleon iron. But for 1 GeV/nucleon iron particles, the stopping power is close to that of 500 MeV/nucleon iron particles. It is 150.4 keV/μm for 1 GeV/nucleon iron particles, whereas 186.3 keV/μm for 500 MeV/nucleon. As a result, the y_F and the ratio of y_F of 1 GeV/nucleon and 500 MeV/ nucleon particles are very close to each other. Consiquently, the 1 GeV/nucleon spectrum is similar to the 500 MeV/nucleon spectrum (Fig. 4.9).

Table 4.2 is the summary of y_F and the ratio of y_F between different site sizes irradiated by iron particles with different energy. The values of y_F and the ratio for the 1 GeV/n iron are smaller than the 500 MeV/n iron. This is because of the smaller stopping power of 1 GeV/n iron and their longer range of δ-rays. There is another factor that may have made the values even smaller. In order decrease the calculation time, we used the detector design that was ideal for 500 MeV/n iron. The wall was not thick enough to stop the δ-rays generated outside of the wall by 1 GeV/n iron. A parallel beam with the diameter of the detector was used in the simulation. If a uniform field and thicker wall had been used, there would be more δ-rays entering the site. If we had used wall thick enough to stop δ-rays generated outside, the number of δ-rays would increase in the thick wall. Both of the changes will increase the δ-ray events, decrease the y_F and increase the ratio, thus enhance the size effect. Further calculations are required to obtain

the results with more accuracy. The detector's response to higher energy particles finally requires experimental calibrations because a practical wall thickness can not increase without limits.

Table 4.2. Lineal energy y_F and the ratio of y_F between different site sizes irradiated by $^{56}Fe^{26+}$ particles. The y_F of 2.5 μm site was taken as 100%.

Energy	Site Size	2.5 μm	0.5 μm	0.1 μm
1000 MeV/n	y_F	139	68.4	18.5
	ratio	100%	49.2%	13.3%
500 MeV/n	y_F	177	91.8	25.3
	ratio	100%	51.9%	14.3%
100 MeV/n	y_F	737	610	375
	ratio	100%	82.8%	50.9%
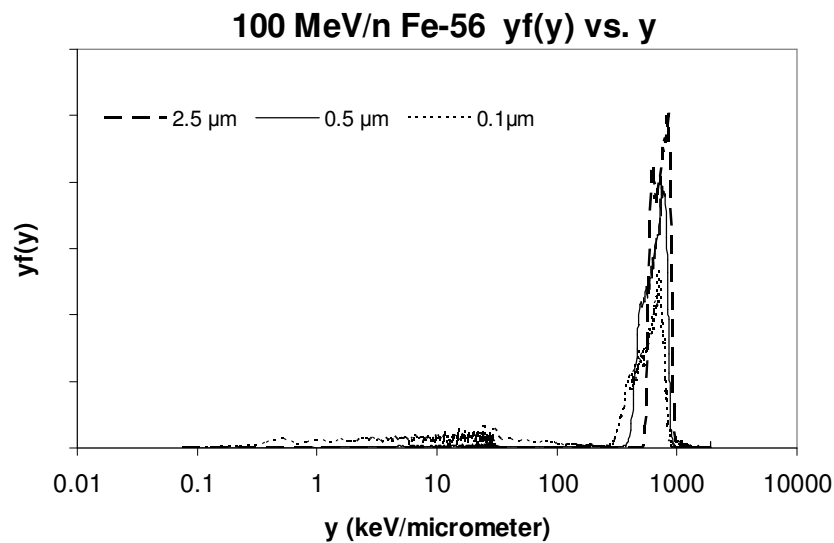
Fig. 4.8. The frequency distribution, $yf(y)$, for a uniform broad beam of 100 MeV/nucleon iron ions irradiating solid walled detectors simulating sites 2.5, 0.5, and 0.1 μm in diameter. The left peak of 2.5 μm diameter site may be caused by backscattering of the inner side of the wall.

1 GeV/n Fe-56 yf(y) vs. y
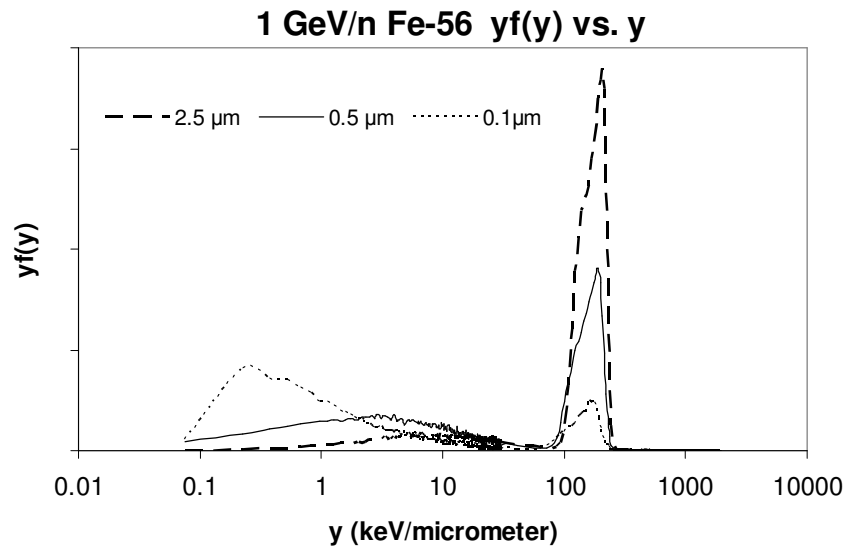
Fig. 4.9. The frequency distribution, $yf(y)$, for a uniform broad beam of 1 GeV/nucleon iron ions irradiating solid walled detectors simulating sites 2.5, 0.5, and 0.1 μm in diameter.

The simulations and comparison of different energy have been done for silicon, oxygen, helium and proton particles. Tables 4.3 to 4.6 are the summary of y_F and the ratio of y_F between different site sizes irradiated by each particle with different energy. It can be seen that oxygen and silicon have obvious y_F changes with the site size. The magnitude of changes for each particle is different. So this detector system is capable of distinguish spectra of mono-energetic HZE isotopes, given enough difference between energies. For helium and proton, the y_F does not change much for different size site. But the profile of the distribution curves changes dramatically from 500 MeV/n to 100 MeV/n (Figs. 4.6 and 4.10). The particles with different energy generate spectra with different shapes, which can be used as information characterizing incident particles.

Table 4.3. Lineal energy y_F and the ratio of y_F between different site sizes irradiated by $^{28}Si^{14+}$ particles. The y_F of 2.5 μm site was taken as 100%.

Energy	Site Size	2.5 μm	0.5 μm	0.1 μm
1000 MeV/n	y_F	40.5	23.2	8.96
	ratio	100%	57.3%	22.1%
500 MeV/n	y_F	52.2	31.0	11.7
	ratio	100%	59.4%	22.4%
100 MeV/n	y_F	189	159	105
	ratio	100%	84.1%	55.6%

Table 4.4. Lineal energy y_F and the ratio of y_F between different site sizes irradiated by $^{16}O^{8+}$ particles. The y_F of 2.5 μm site was taken as 100%.

Energy	Site Size	2.5 μm	0.5 μm	0.1 μm
1000 MeV/n	y_F	13.7	9.14	4.75
	ratio	100%	66.7%	34.7%
500 MeV/n	y_F	17.7	12.3	6.36
	ratio	100%	69.5%	35.9%
100 MeV/n	y_F	57.5	50.0	35.7
	ratio	100%	87.0%	62.1%

Table 4.5. Lineal energy y_F and the ratio of y_F between different site sizes irradiated by $^4He^{2+}$ particles. The y_F of 2.5 μm site was taken as 100%.

Energy	Site Size	2.5 μm	0.5 μm	0.1 μm
1000 MeV/n	y_F	0.980	0.883	0.779
	ratio	100%	90.1%	79.5%
500 MeV/n	y_F	1.23	1.11	1.00
	ratio	100%	90.2%	81.3%
100 MeV/n	y_F	3.44	3.16	2.87
	ratio	100%	91.9%	83.4%

Table 4.6. Lineal energy y_F and the ratio of y_F between different site sizes irradiated by protons. The y_F of 2.5 μm site was taken as 100%.

Energy	Site Size	2.5 μm	0.5 μm	0.1 μm
1000 MeV/n	y_F	0.286	0.289	0.229
	ratio	100%	101%	80.1%
500 MeV/n	y_F	0.339	0.344	0.279
	ratio	100%	101%	82.3%
100 MeV/n	y_F	0.889	0.835	0.848
	ratio	100%	93.9%	95.4%

Same Stopping Power Particles

It is of great importance for the detector system to have different response to particles with same stopping power. Of the simulated particles, some have very close stopping power. The data of these particles can help us to study the ability of the detector system to characterize HZE particles. Table 4.7 summarizes these particles' LET in water, y_F and the ratio of y_F between different site sizes.

There are three pairs of particles being compared. For the first two pairs of HZE particles, not only the y_F defers from each other, but also the y_F changes obviously in different ratio. It is easy to tell them apart. For 1 GeV/nucleon helium particles and 100 MeV/nucleon protons, the values are close to each other. But their spectra have unique characters. The spectrum of 1 GeV/nucleon helium is similar to Fig. 4.5. The spectrum of 100 MeV/nucleon protons is shown in Fig. 4.10. It is very easy to distinguish them.
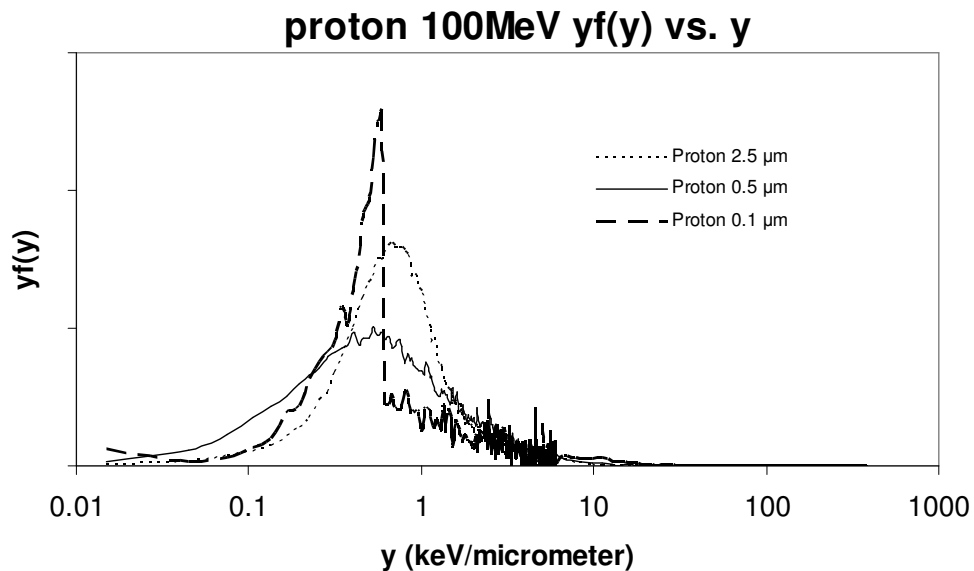
Fig. 4.10. The frequency distribution, $yf(y)$, for a uniform broad beam of 100 MeV/nucleon protons irradiating solid walled detectors simulating sites 2.5, 0.5, and 0.1 μm in diameter.

Table 4.7. LET, lineal energy y_F and the ratio of y_F between different site sizes of particle with similar LET. The y_F of 2.5 µm site was taken as 100%.

Particle	Energy MeV/n	LET keV/µm	y_F /ratio	2.5 µm	0.5 µm	0.1 µm
$^{56}Fe^{26}$	1000	150	y_F	139	68.4	18.5
			ratio	100%	49.2%	13.3%
$^{28}Si^{14+}$	100	144	y_F	189	159	105
			ratio	100%	84.1%	55.6%
$^{28}Si^{14+}$	1000	43.6	y_F	40.5	23.2	8.96
			ratio	100%	57.3%	22.1%
$^{16}O^{8+}$	100	47.0	y_F	57.5	50.0	35.7
			ratio	100%	87.0%	62.1%
$^{4}He^{2+}$	1000	0.890	y_F	0.980	0.883	0.779
			ratio	100%	90.1%	79.5%
proton	100	0.731	y_F	0.889	0.835	0.848
			ratio	100%	93.9%	95.4%

It is inspiring to prove that this multi-size detector system is capable of characterizing particles with same stopping power. Obviously, the detectors can also provide information that a normal proportional counter can do, such as dose, dose mean and mean lineal energy. It certainly can provide more routes to determine the dose and characterize the incident particle. A detector system with a similar design can be built to study further its practicability.

It should be mentioned that the calculated mean lineal energy is larger than LET in some situations, especially with low energy. One of the major reasons is the δ-ray effect and the re-entry component of the wall effect. For 100 MeV/nucleon particles with large stopping power, this is more apparent. However, the wall effect may not fully explain

how the averaged lineal energy can be larger than LET. Further study is required to provide more information and a detailed explanation.

Proton and Helium Spectra

In Fig. 4.6, the 0.1 μm spectrum shows a large event distribution peak at about 0.3 keV/μm and a sharp falling edge. In this small site, protons can go through the site with small possibility of producing a δ-ray. So the proton peak can be observed. The sharp edge indicates the maximum energy deposition by the protons going through from the center of the site. Since an electron has the same stopping power as a proton, electrons going 'straight' through the site also contribute to the proton peak. Since an electron may travel longer tortuous route in the site, it may deposit more energy than a proton. The events with lineal energy greater than 0.3 keV/μm are mainly due to scattering electrons (maybe together with a proton). The similar mechanism happens to ^{4}He particles. But the effect is weakened by ^{4}He particles larger stopping power. More δ-rays smooth the peak and the edge of the 0.1 μm curve (Fig. 4.5).

Using the lineal energy and size of the site (mean chord length, $\bar{l}$), we can derive the energy of the events of the peak. It indicates that these events are of *single ionization events*. It means only one ionization happens in the site when the particle goes through the site, probably with a few excitations contributing a few more eV of energy. The events at the right side of the peak have multiple ionizations. The single ionization events can also be observed in 0.5 μm site. The small peak on the left in Fig. 4.6 is composed of single and two ionizations events. The position shifts left because the site size increases and makes the lineal energy smaller. In Fig. 4.5, the peak for 0.1 μm site are also composed of single and double ionization events.

When the energy changes to 100 MeV/n, this particular character of proton and helium spectrum subsides. In Fig. 4.10, the peak of 0.1 μm is composed of both single and double ionization events. The peak for 0.5 μm site disappears. The same thing happens for helium particles (Fig. 4.11). It is because the stopping power is much larger for these 100 MeV/n particles. The single and double ionization events are substituted by

multiple ionizations. This phenomenon happens only for proton and helium. We can further anticipate that in a mix field of various particles and wide energy range, the whole proton and helium spectrum may still keep the evidence of this property. That will be helpful for characterizing incident particles. Further simulations and experiment work are needed to prove this hypothesis.
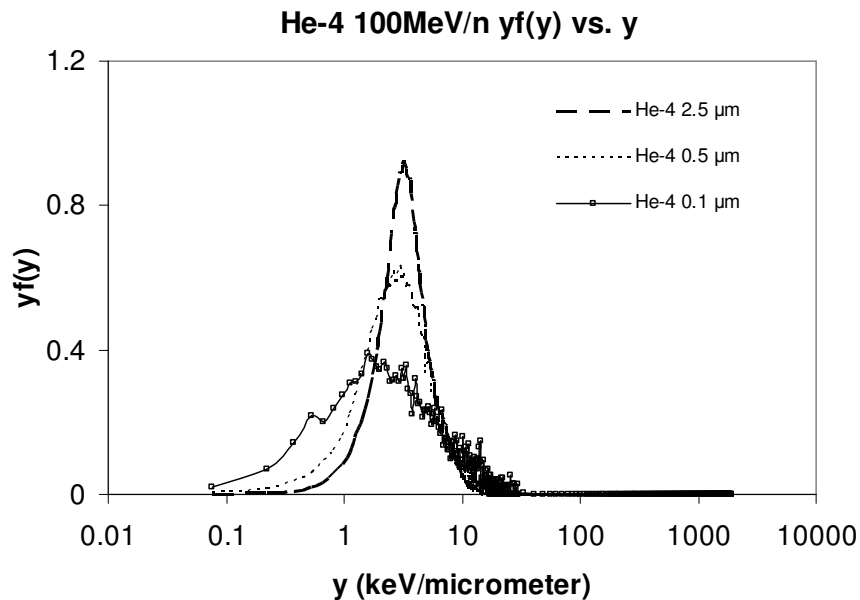
Fig. 4.11. The frequency distribution, $yf(y)$, for a uniform broad beam of 100 MeV/nucleon helium ions irradiating solid walled detectors simulating sites 2.5, 0.5, and 0.1 μm in diameter.

Consistency of Size Effect

It is worthwhile to check if the detector system shows consistent size effect to different energy particles. If there is constancy in the data, the detector system can be put into practical use for a much wider range of particles and energy with more confidence. For the HZE particles, the size effect becomes weakened as the size increases, and the energy decreases. The y_F of 100 MeV/nucleon particles changes less between the

different size sites than that of 500 MeV/n particles. This trend is true for all particles but protons. Fig. 4.12 shows the consistency of the data.

The y_F of 1 GeV and 500 MeV protons in 0.5 μm site increases relative to the 2.5 μm site. Firstly, they have very low lineal energy, which is close to that of the δ-rays. So for protons, the distribution of δ-rays contributes more to the y_F than for heavy ions. Secondly, they have a very low production of δ-rays. As a result of smaller number of ionizations in the 0.5 μm site, the bell shape curve of δ-ray distribution becomes widened (Figs. 4.6 and 4.10), and the proton's lineal energy distribution does not change much. This causes the slight increase of y_F. For 100 MeV protons in 0.5 μm site, the production of δ-rays increases. The size effect again dominates the change of y_F in 0.5 μm site.

Size Effect vs. z of Incident Particle
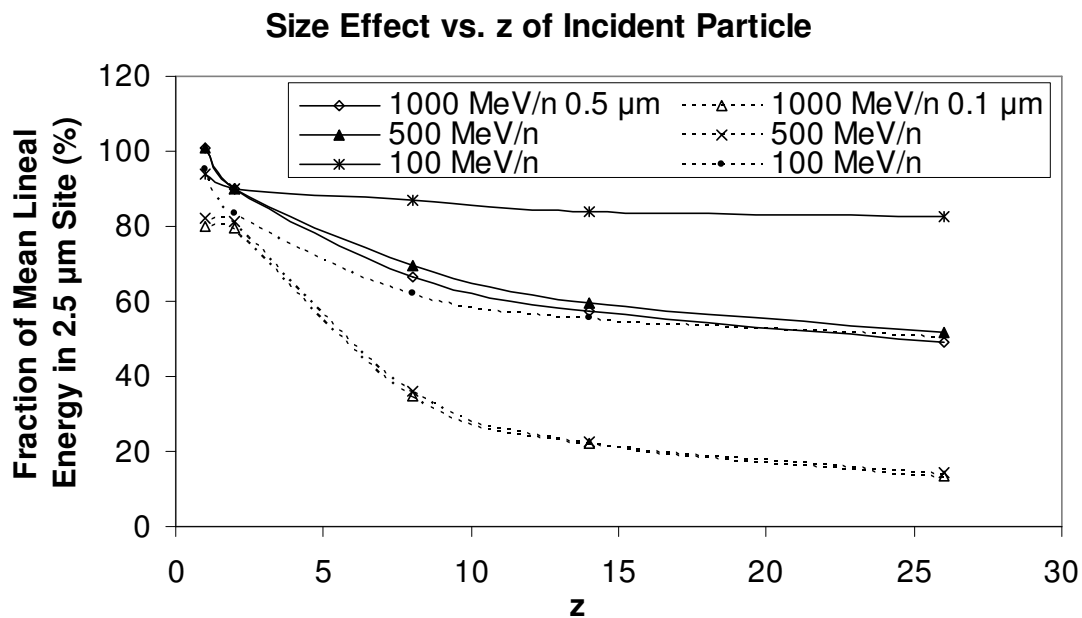

Fig. 4.12. Size effect of particles of different z in 0.5 and 0.1 μm site. The energy used was 1 GeV/n, 500 MeV/n and 100 MeV/n. The ordinate is the ratio of y_F, with y_F of 2.5 μm site as the denominator. The abscissa is the charge of the primary particles. The particles involved are hydrogen, helium, oxygen, silicon and iron, from left to right.

Mixed Spectrum

Practically, the detector system will be used in an isotropic mix field. The system's ability of characterizing particles in such a field shall be studied by combining more simulation results of various particles in a wider energy range. We will only have a brief discussion based on the current results.

The collection of distribution curves in 2.5 μm diameter site was shown in Fig. 4.13. The peak of each particle has its mean lineal energy and height. When the measurement is done in a mix field, the peaks will overlap each other. For example, the peak of 500 MeV/nucleon iron overlaps with 100 MeV/nucleon silicon, and the peak of 1 GeV/nucleon and 500 MeV/nucleon silicon overlap with 100 MeV/nucleon oxygen. But we can predict that for each particle in a wide energy range, the whole spectrum will be a bell shape curve with different mean lineal energy and peak height. Considering the mean lineal energy, element abundance in cosmic ray, and the changes with site size, we may have enough information to distinguish them from each other. Again, in 0.1 μm diameter site, the distribution of the primary particle and δ-rays is distinct for each particle (Figs. 4.14 and 4.15). The bell shape curves may have dramatic changes, which are helpful to characterize the particles.

If two detector systems are used with and without shielding, the fragment generated in the shielding will modify the profile of the spectrum. This will also helpful to get information on the composition of the field.
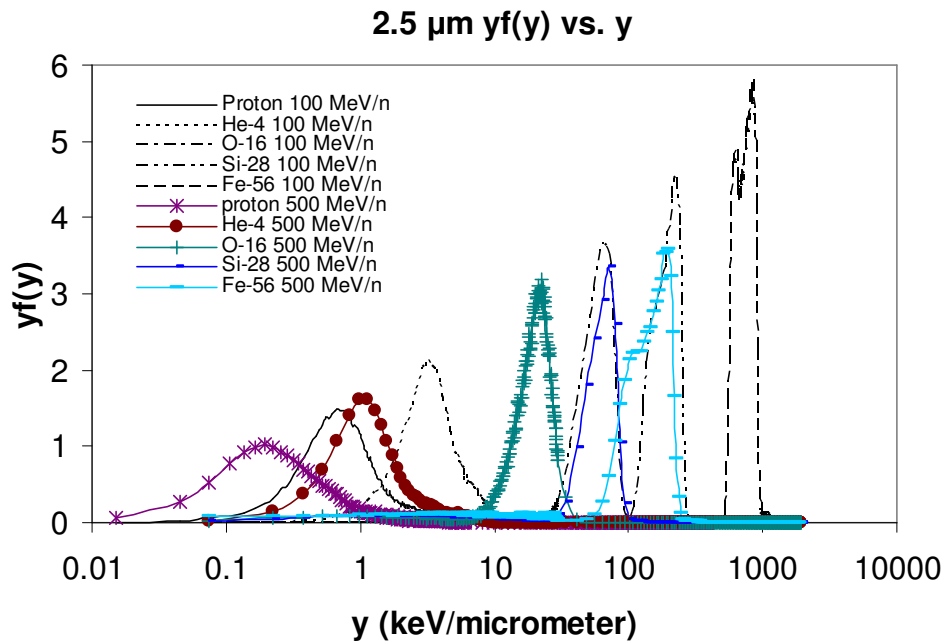
Fig. 4.13. The frequency distribution, *y*f(*y*), of 100 and 500 MeV/nucleon ions irradiating solid walled detectors simulating sites 2.5 μm in diameter.
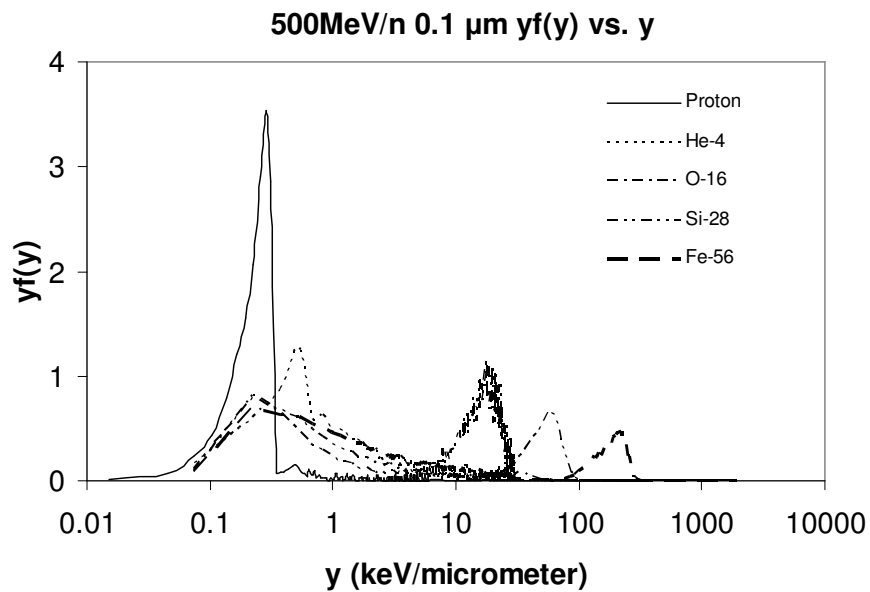
Fig. 4.14. The frequency distribution, *y*f(*y*), of 500 MeV/nucleon ions irradiating solid walled detectors simulating sites 0.1 μm in diameter.

100MeV/n 0.1 μm yf(y) vs. y
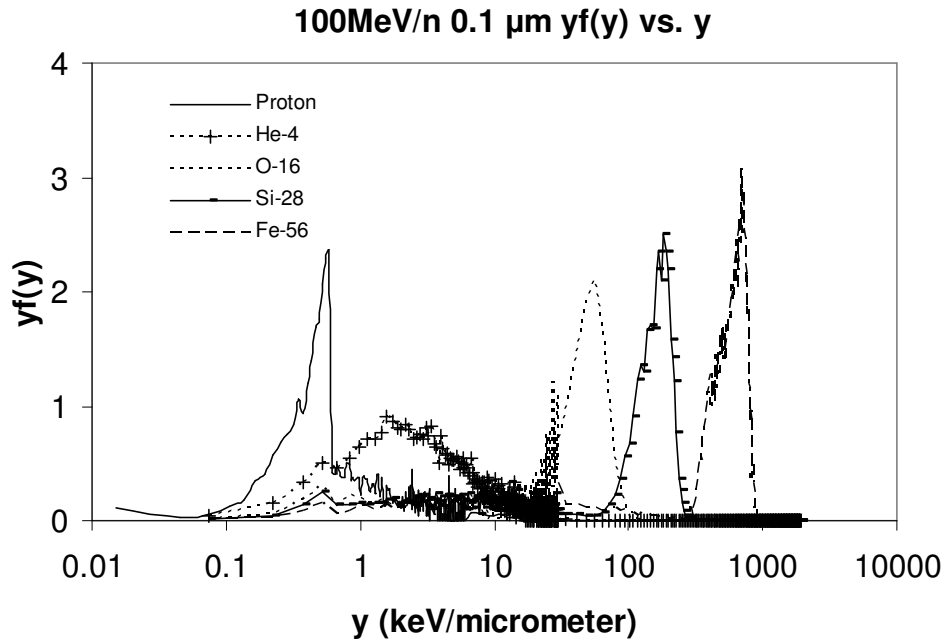
Fig. 4.15. The frequency distribution, $yf(y)$, of 100 MeV/nucleon ions irradiating solid walled detectors simulating sites 0.1 μm in diameter.

Error of Data

Several (n=7) calculations have been run to get the standard deviation of y_F. Each calculation uses 100,000 particles with different random seeds. Due to shortage of CPU time, only the errors of iron particles were calculated. The y_F values with error are 176.82 ± 0.39, 91.83 ± 0.30, 25.43 ± 0.28 keV/μm for 2.5, 0.5 and 0.1 μm diameter size, respectively. The stochastic error is within 1%. The y_F of all the other particles used in the previous sections was obtained from only one calculation. From the small variance obtained for iron, it is reasonable to assume the y_F values of other calculations are close to the mean value of multiple calculations.

CHAPTER V

CONCLUSIONS

This is a first attempt at Monte-Carlo simulations of a multiple size detector system used for microdosimetry measurement of space radiation. Size effect of a series of solid walled detector was calculated with HZE particles as well as helium and hydrogen ions.

Firstly, it is worthy to declare that GEANT4 toolkit is capable of simulating interaction of materials and HZE particles. It is also capable of simulating almost all the interaction related to cosmic ray dosimetry, such as neutron, electron and γ-ray radiations. It can also simulate a complex field. So, this study is a good start to use GEANT4 in cosmic radiation microdosimetry study.

The data analysis techniques can be applied in experimental data analysis. The skills of normalization, start point treatment and spectrum welding are also used in experiments. The simulation results can help to determine some measurement requirements, such as gas gain value, measurement time, the lowest energy signal of interest and so on.

In Monte-Carlo toolkit GEANT4, a series of approximations were employed. The physics model (processes) used in the simulations has the greatest impact on data accuracy. Although calibration is needed for the absolute dose evaluation, the simulation results still have remarkable sensitivity to show the size effect by using the standard electromagnetic process. The 2 mm wall thickness can not provide charged particle equilibrium for particles with energy greater than 500 MeV/nucleon. Further experimental calibration is necessary for the high energy particles. The 0.01 mm cut value is an acceptable approximation for the present geometry design and physics processes. In case more calculation power is available, all these approximation parameters can be improved to get results with better accuracy.

Besides the standard deviation, there are errors introduced by physics models and data libraries used in GEANT4. An experiment measurement is necessary to study the performance of such a detector system in an HZE particle field. The experiment can also

provide foci on which we can put emphasis when simulating a uniform wide energy field. Comparison of the calculation and the experimental results is helpful to understand the size effect and accuracy of the simulations.

The site size was chosen as 2.5, 0.5 and 0.1 μm. It has been shown that such a group of size functions very well to manifest size effect for various particles in a wide energy range. The count rate ratio for these three detectors is 625:25:1. In the simulations the fluence for each size detector is different. The ratio of fluence is about 1:11:43 for 2.5 and 0.5 and 0.1 μm diameter site. It was not necessary to shoot more particles at the small detectors in order to get good statistics. Although the fluence used is in favor of the small detectors, the calculation results still show that such a group of size have acceptable ratio of counting rate in practical use.

The ability of the detector system to characterize these radiations is prominent. By analyzing the spectra from the three detectors, we can easily distinguish mono-energetic particles, even when they have the same stopping power. The characterizing ability is consistent for particles with different mass and energy. The light particles such as proton and helium also have their unique spectral characteristics. We shall predict that the detector system is capable of characterizing particles in a wide energy range. The idea of using size effect to characterizing HZE particles when measuring the dose is shown to be feasible. This encourages the attempt of construction of such a detector system. Further simulations of particles with more variety of mass and energy are necessary to study the characterizing ability in the uniform complex cosmic ray field.

REFERENCES

Agostinelli S, Allison J, Amako K, Apostolakis J, Araujo H. Geant4 - a simulation toolkit. Nuclear Instruments and Methods in Physics Research A 506: 250-303; 2003.

Allison J, Amako K, Apostolakis J, Araujo H, Arce Dubois P. Developments and applications. IEEE Transactions on Nuclear Science 53: 270-278; 2006.

Attix FH. Introduction to radiological physics and radiation dosimetry. New York: John Wiley & Sons; 1986.

Braby LA, Johnson GW, Barthe J. Practical considerations in the design and construction of tissue-equivalent proportional counters. Radiation Protection Dosimetry 61: 351-379; 1995.

Clay R, Dawson B. Cosmic bullets - High energy particles in astrophysics. Sydney, Australia: Allen and Unwin; 1997.

Fano U. Note on the Bragg-Gray cavity principle for measuring energy dissipation. Radiation Research 1: 237-239; 1954.

Glass WA, Braby LA. A wall-less detector for measuring energy deposition spectra. Radiation Research 39: 230-240; 1969.

Guetersloh SB, Borak TB, Taddei PJ, Zeitlin C, Heilbronn L, Miller J, Murakami T, Iwata Y. The response of a spherical tissue-equivalent proportional counter to defferent ions having similar linear energy transfer. Radiation Research 161: 64-71; 2004.

ICRP. International Commission of Radiation on Radiological Protection. Recommendations of the International Commission on Radiological Protection (ICRP Publication 60, Annals of the ICRP, Vol. 21, No. 1-3). New York: Pergamon Press; 1991.

ICRU. International Commission on Radiation Units and Measurements, Microdosimetry (ICRU report 36). Bethesda, MD: ICRU; 1983.

Kaplan I. Nuclear physics. Cambridge, MA: Addison-Wesley Publishing Company, Inc.; 1956.

Kellerer AM. An assessment of wall effects in microdosimetric measurements. Radiation Research 47: 377-386; 1971a.

Kellerer AM. Considerations on the random traversal of convex bodies and solutions for general cylinders. Radiation Research 47: 359-376; 1971b.

Kellerer AM. Event simultaneity in cavities. Theory of the distortions of energy deposition in proportional counters. Radiation Research 48: 216-233; 1971c.

Metting NF, Rossi HH, Braby LA. Microdosimetry near the trajectory of high-energy heavy ions. Radiation Research 116: 183-195; 1988.

Mewaldt RA, Davis AJ, Binns WR, Nolfo de GA, George JS, Isreal MH, Leske RA, Stone EC, Wiedenbeck ME, von Rosenvinge TT. The cosmic ray radiation dose in interplanetary space - Present day and worst-case evaluations. 29th International Cosmic Ray Conference Pune 00: 101-104; 2005.

NCRP. National Council on Radiation Protection and Measurements. Guidance on radiation received in space activities (NCRP 98). Bethesda, MD, USA: NCRP; 1989.

NCRP. National Council on Radiation Protectoion and Measurements. Radiation protection guidance for activities in low-earth orbit (NCRP 132). Bethesda, MD: NCRP; 2000.

Rayadurgam S. Design of a wall-less proportional counter for microdosimetry in nanometer dimensions. In: M.S. thesis. College Station, TX: Texas A&M University; 2005.

Rossi HH, Biavati MH, Gross W. Local energy density in irradiated tissue. 1. Radiological significance. Radiation Research 15: 431-439; 1961.

Rossi HH, Rosenzweig W. A device for the measurement of dose as a function of specific ionization. Radiology 64: 404-411; 1955.

Rossi HH, Zaider M. Microdosimetry and its applications. New York: Springer-Verlag; 1996.

VITA

Xudong Wang received his Bachelor of Science degree in material science from Lanzhou University, Lanzhou, China in 1997. He entered the Nuclear and Particle Physics program at the Institute of Modern Physics, Chinese Academy of Sciences in 2000, and he received his Master of Science degree in June 2003. He entered the Health Physics program at the Texas A&M University in August 2004. He may be reached at Nuclear Engineering Dept, Texas A&M University, 3133 TAMU, College Station, TX 77843-3133. His email address is xdwang@tamu.edu.